SANDIA REPORT
SAND2022-7150
Printed June 2022

Instrumented Photovoltaic Modules for Environmental Characterization and Simulation Model Validation

Matthew R. Phillips (1514), James Y. Hartley (1514), Ashley M. Maes (1512), and Charles D. Robinson (8924)

Prepared by
Sandia National Laboratories
Albuquerque, New Mexico
87185 and Livermore,
California 94550

Issued by Sandia National Laboratories, operated for the United States Department of Energy by National Technology & Engineering Solutions of Sandia, LLC.

Available to DOE and DOE contractors from
U.S. Department of Energy
Office of Scientific and Technical Information
P.O. Box 62
Oak Ridge, TN 37831

Telephone: (865) 576-8401
Facsimile: (865) 576-5728
E-Mail: reports@osti.gov
Online ordering: http://www.osti.gov/scitech

Available to the public from
U.S. Department of Commerce
National Technical Information Service
5301 Shawnee Rd
Alexandria, VA 22312

Telephone: (800) 553-6847
Facsimile: (703) 605-6900
E-Mail: orders@ntis.gov
Online order: https://classic.ntis.gov/help/order-methods/

ABSTRACT

Photovoltaic modules are subjected to various mechanical stressors in their deployment environments, ranging from installation handling to wind and snow loads. Damage incurred during these mechanical events has the potential to initiate subsequent degradation mechanisms, reducing useful module lifespan. Thus, characterizing the mechanical state of photovoltaic modules is pertinent to the development of reliable packaging designs.

In this work, photovoltaic modules with strain gauges directly incorporated into the module laminate were fabricated and subjected to mechanical loading to characterize internal strains within the module when under load. These experimental measurements were then compared against results obtained by high-fidelity finite-element simulations.

The simulation results showed reasonable agreement in the strain values over time; however, there were large discrepancies in the magnitudes of these strains. Both the instrumentation technique and the finite-element simulations have areas where they can improve. These areas of improvement have been documented.

Despite the observed discrepancies between the experimental and simulated results, the module instrumentation proved to be a useful gauge in monitoring and characterizing the mechanical state. With some process improvements, this method could potentially be applied to other environments that a photovoltaic module will encounter in its lifetime that are known to cause damage and degrade performance.

ACKNOWLEDGEMENTS

The authors would like to acknowledge Brantley Mills and Joshua Stein for programmatic guidance and review of this report; Nate Smith (9144) for assistance with LabView data acquisition scripts; and Mike Rowell (mike.rowell@d2solar.com) and Duncan Harwood (duncan.harwood@d2solar.com) at D2 Solar LLC for custom module fabrication.

Sandia National Laboratories is a multi-mission laboratory managed and operated by National Technology and Engineering Solutions of Sandia, LLC., a wholly owned subsidiary of Honeywell International, Inc., for the U.S. Department of Energy's National Nuclear Security Administration under contract DE-NA-0003525

Funding was provided as part of the Durable Modules Consortium (DuraMAT), an Energy Materials Network Consortium funded by the U.S. Department of Energy, Office of Energy Efficiency and Renewable Energy, Solar Energy Technologies Office. The views expressed in the report do not necessarily represent the views of the DOE or the U.S. Government. The U.S. Government retains a nonexclusive, paid-up, irrevocable, worldwide license to publish or reproduce the published form of this work, or allow others to do so, for U.S. Government purposes.

CONTENTS

LIST OF FIGURES

LIST OF TABLES

This page left blank

EXECUTIVE SUMMARY

Understanding the mechanical state of photovoltaic modules in the field is pertinent to the development of reliable packaging designs to enable cost-effective electricity production from photovoltaics. However, these data are limited primarily to standard experiments conducted in laboratories, which may not account for real-world effects. Thus, *in-situ* measurements of the module's mechanical state are needed to better assess module reliability in the field. High-fidelity computational simulations can augment these data, but both the proposed instrumentation method and the simulations must be validated.

First, three full-sized photovoltaic modules were constructed with in-situ instrumentation to validate the *in-situ* sensor lamination process. One additional module was left without instrumentation to serve as the control. The three instrumented modules were each used to elucidate certain physical phenomena anticipated during the mechanical test, like symmetric deformations, junction box effects, and lamina-dependent strains. Displacement, electroluminescence, and strain gauge data were collected during the four experiments. The module dimensions and bill of materials were selected such that the finished modules would best represent both commercially available modules and existing simulation models to improve the applicability of the results.

Instrumenting a photovoltaic module with additional sensors required more labor than leaving a module uninstrumented. Care had to be taken to prevent bubbles or cell cracking near wires protruding from the sensors and at locations where wire bundles intersected, which may otherwise degrade electricity production efficiency and accelerate premature failure. Also, soldering gauges to the brittle silicon cells is not ideal since it may increase the likelihood of cell cracking and because the surrounding encapsulant sheets are sensitive to heat. For these reasons, among others, gauges at select locations were laminated between the encapsulant and backsheet layers rather than directly on the cells. In practice, in-situ measurements at these locations would likely interfere less with the electricity production than those laminated directly to the cell.

Mechanical tests were performed on the four constructed modules. The controlled test allowed for extrinsic measurements, such as the displacement field, to be mapped to intrinsic values of strain for uniform pressure loads applied to the module. Since the full module face was accessible during the tests, electroluminescence images were taken to ensure that the pressure cycle was severe enough to induce cell cracking. Three pressures were selected during the load cycle where the pressure would remain constant for twenty minutes to observe module relaxation behavior taking place because of geometric nonlinearities or hysteretic material behavior. Both the displacement and strain measurements confirmed that the module relaxes during each of the pressure-hold intervals.

High-fidelity finite-element simulations were also developed and validated against the experimental measurements. The finite-element model exploited quarter symmetry of the module to reduce computational costs. Compromises were made in representing the physical module in the simulation to ease with mesh generation. Although these differences incidentally attributed to larger theoretical stiffnesses of the frame than anticipated, additional simulations with a more representative geometry suggested that the material property selection had a greater influence on the module deformation during loading.

To account for the relaxation behavior observed in the experiments, the simulations represented the polymer encapsulant as a viscoelastic material. The relaxation trends of the simulated displacements and strains matched those observed in the experiments, but the

simulations predicted smaller magnitudes than was measured experimentally. The encapsulant material model used in the simulations was taken from a comparable encapsulant material found in the literature, and thus was not identical to the encapsulant used in the module construction. It is expected that repeating the high-fidelity simulation with material properties from the true encapsulant material would provide closer agreement with the experimental observations.

Additional simulations were conducted to quantify the effects of viscoelastic versus elastic material models for the encapsulant and edge sealant components. These found that an elastic material model for the edge sealant is suitable for the given photovoltaic panel to reduce computational costs, although the viscoelastic representation of the encapsulant material is necessary.

Overall, the proposed *in-situ* method for characterizing the mechanical state of a photovoltaic module is a useful method and could be expanded to predict the stress-strain response from other environments that a photovoltaic module will encounter in its lifetime, including high-frequency cyclic pressure loadings, hailstone impacts, and abuse loading from transportation and installation environments. Moreover, the high-fidelity simulations are a useful supplement to the experimental measurements, but they require accurate material characterizations of each module component. Both the in-situ measurements and the finite-element simulations can be improved in future works.

ACRONYMS AND DEFINITIONS

Abbreviation	Definition
PV	Photovoltaic
EL	Electroluminescence
PL	Photoluminescence
IR	Infra-red
EVA	Ethylene-vinyl acetate
PDMS	Polydimethylsiloxane
PET	Polyethylene terephthalate

1. INTRODUCTION

Crystalline photovoltaic (PV) modules are subjected to various mechanical stressors in their deployment environments, ranging from installation handling to wind and snow loads on the glass surface. Contained within the module are the brittle silicon cells, which convert sunlight to electricity. The deformation of the module resulting from the environmental loadings has the potential to reduce the lifespan of the module by cracking the silicon cells, reducing the electrical output over time [1].

The module package, composed of glass, encapsulant, and a backsheet, is designed to protect the fragile silicon cells from damage [2,3]. However, manufacturers must balance module survivability with cost minimization to ensure photovoltaic electricity production is competitive with other sources in the market.

Thus, understanding the mechanical state of PV modules in the field is pertinent to the development of reliable packaging designs to enable cost-effective electricity production from photovoltaics.

Full-scale mechanical stress tests have been developed over the years to improve and certify PV module designs [4]. These tests are typically conducted in controlled laboratory environments where the loading conditions are known. One common testing procedure is to apply a quasistatic uniform pressure load on the glass surface of a module to measure the module deformation and quantify cell cracking [1,4,5]. Several methods to apply a uniform load have been tested, such as placing fixed weights directly on the glass, using an array of suction cups to push or pull on the surface, and, more recently, sealing the edges of the module in a vacuum chamber and using air pressure to apply the uniform load [4,6].

Despite the development of mechanical testing procedures, measurements have still been limited primarily to extrinsic values, like discrete displacements on accessible surfaces, and may not account for real-world effects. Computational simulations can substantially augment the interpretation of these test data, by providing information about the internal state of components while undergoing external forcing. However, the integration of testing and simulation data is still lacking, since simulated results can only be validated against extrinsic quantities (i.e., displacements at specific points) instead of the actual intrinsic quantities (i.e., stress and strain) leading to damage and degradation. Thus, *in-situ* measurements of the module's mechanical state are needed to better assess module reliability.

Strain gauges laminated permanently within the module lamina offer a simple *in-situ* method to monitor the intrinic mechanical state of a PV module. By design, strain gauges are nominally flat, so they are expected to be minimally intrusive. They are also advantageous as an *in-situ* measurement device since they provide continuous, high precision measurements [1]. Before deploying instrumented PV modules in the field; however, the accuracy of the in-situ method must be assessed in controlled mechanical tests [1,5].

High-fidelity computational simulations can augment these data, but both the proposed instrumentation method and the simulations must be validated. In previous high-fidelity computations of PV modules, all components were regarded as linear elastic [1,5]. However, observations from experimental testing showed that module relaxation occurred when subjected to a uniform pressure load of 2400 Pa [1]. While elastic material models are more easily characterized and computationally cheap, there is growing evidence that viscoelastic behavior of the polymer components are needed for more accurate predictions of the module's mechanical state [2].

In this work, strain gauges were embeded into custom built, commercially representative photovoltaic modules and subjected to mechanical loading to obtain direct, localized data during testing. The materials and processing conditions of these modules are known fully, so that a direct correlation to model inputs can be established. The experimental measurements were then compared against results obtained by an improved high-fidelity finite-element simulation with a viscoelastic encapsulant material. The goals of this project are the following: 1) Test an *in-situ* measurement concept that improves upon current practices for module characterization in thermal-mechanical environments; 2) Collect high-fidelity module state information for model validation.; and 3) Validate the finite-element simulation.

2. INSTRUMENTED MODULE HARDWARE

The instrumented modules used in this study were fabricated with full control over the dimensions, material selection, and assembly. These parameters were selected intentionally so that the finished modules would best represent both commercially available modules and existing simulation models to improve the applicability of the results. The final module design was constructed with 60 monocrystalline, 5-busbar cells, Solite glass, a Mitsui® EVA encapsulant, and a PET backsheet. The cross-section of the module frame is shown in Figure 2-1, with a total height of 45 mm and a lower flange width of 35 mm. The glass module was made with dimensions 1656 x 991 x 2.8 mm[1]. Figure 2-2 shows a sketch of the module layers. A silicone-based sealant was used to secure the module in the frame. Frame fastening[2] was accomplished with corner keys. Samples of all module components and materials were retained for mechanical characterization testing.

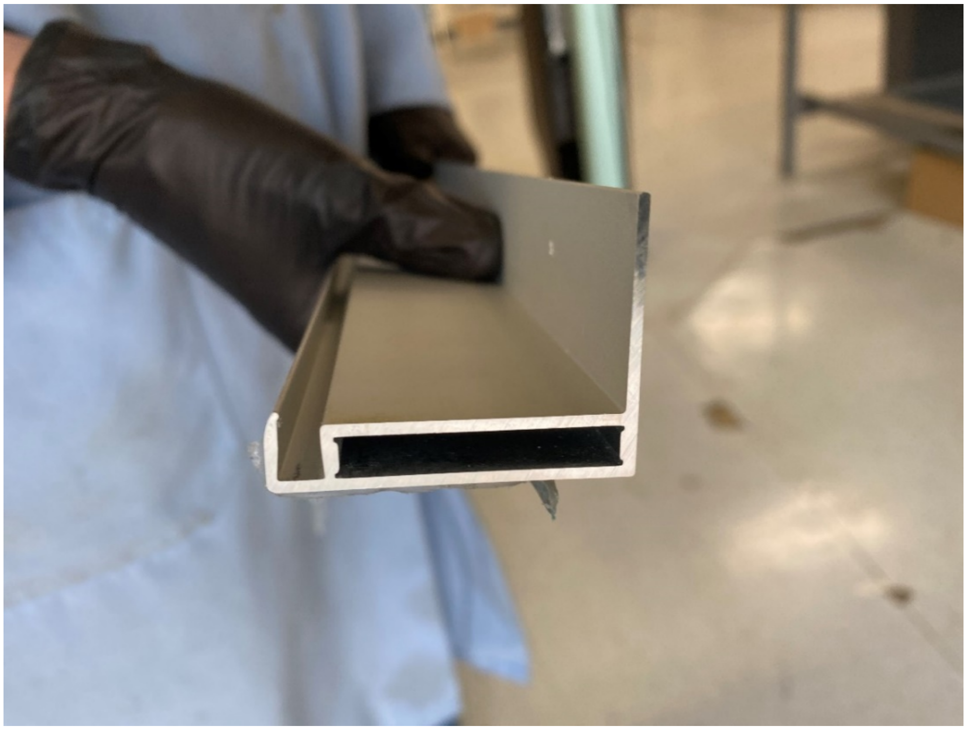

Figure 2-1: Instrumented module frame channel cross-section held sideways.

---

[1] Initial specifications required 3.2 mm glass, but final products contained 2.8 mm glass due to an assembly error

[2] Frames channel dimensions were optimized for 3.2 mm glass, so extra sealant was utilized to form the frame to laminate bond. Additionally, corner keys were observed to be loose fitting, potentially specified for a different frame design than used, with 30 mm x 3.7 mm insertion dimensions vs. frame internal channel dimensions of 34.5 mm x 5.2 mm. Test results should be interpreted with these observations in context.

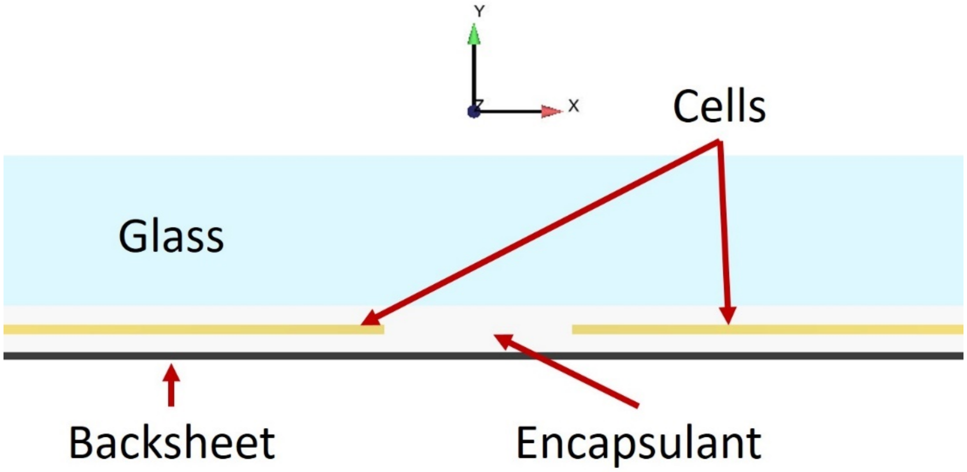

Figure 2-2: Cross-section of photovoltaic panel components.

2.1. Instrumentation

Three varieties of strain gauges were selected for this study: HBM model numbers 1-LY66-10/350, 1-LY61-10/350, and 1-XY101-6/350. Datasheets for each gauge are reprinted in Appendix A. Most gauges were directly adhered to cell back faces using HBM X280 adhesive, a 2-part epoxy recommended by the manufacturer [7], except for select gauges which were directly laminated between the rear encapsulant and backsheet to deliberately assess the effects of not mounting them to a rigid substrate. A summary of instrumentation-related selections and considerations is shown in Table 1.

Table 1: Selected Instrumentation Specifications

Item	Description	Comments
1-LY66-10/350	Single axis strain gauge, temperature expansion coefficient matched to silica (0.5 ppm/K)	Sized to fit between cell busbars in any orientation. Best available temperature match to silicon substrate (2.8 ppm/K)
1-LY61-10/350	Single axis strain gauge, temperature expansion coefficient matched to steel (10.8 ppm/K)	Same as previous except temperature matched to steel. Selected due to limited availability of 1-LY66-10/350 gauges.
1-XY101-6/350	Dual axis strain gauge, temperature expansion coefficient matched to silica (0.5 ppm/K)	Sized to fit between cell busbars in any orientation. Best available temperature match to silicon substrate (2.8 ppm/K)
X280 adhesive	2-part epoxy-resin adhesive	-200°C to +280°C temperature rating. Selected to survive lamination conditions up to 150°C

2.2. Data objectives and instrumentation layout designs

Project funding was sufficient to build four custom modules. Each module had the same overall architecture but different instrumentation configurations. Instrumentation locations were thus divisible among the modules, to reduce the total number of gauges included in each module, which simplified wiring and allowed all quantities to be collected with some redundancy. The key data objectives for the set of instrumented modules are summarized in the following list.

1. Confirm symmetry across module quadrants
2. Assess effects of junction box on nearby cell strain
3. Probe module short and long dimension strain quantities over time, including cells with:
    a. Maximum tensile (positive) strain
    b. Maximum compressive (negative) strain
    c. Neutral (near 0) strain
    d. Reversals in strain sign (positive to negative) on the same cell
4. Establish a control module
5. Assess effect of gauge placement layer within the laminate
6. Assess module-to-module variability

Module gauge layouts are summarized in Figure 2-3, to satisfy the above objectives using as few modules as possible and placed in relation to the key strain features observed in preliminary simulation results as shown in Figure 2-4. It was desired to laminate strain gauges in locations predicted to attain high strain magnitudes, to validate key simulated features and avoid sensitivities of exact gauge placements, which would be more pronounced in areas of lower strain or near sharp gradients.

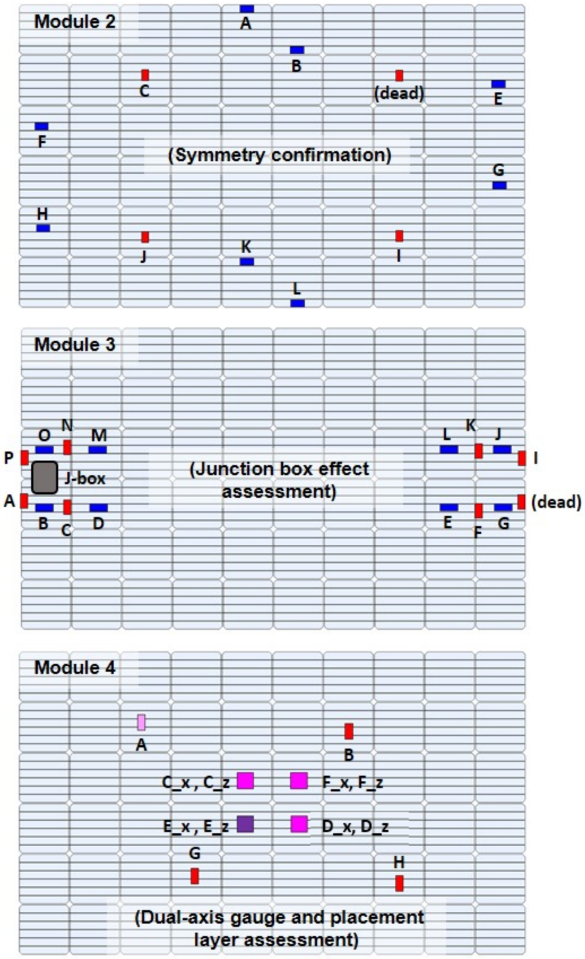

Figure 2-3: Strain gauge layouts for the three instrumented photovoltaic modules. Horizontal blue gauges measure the strain in the x-direction. Vertical red gauges measure the strain in the z-direction. Square gauges measure the strain in both the x- and z-directions.

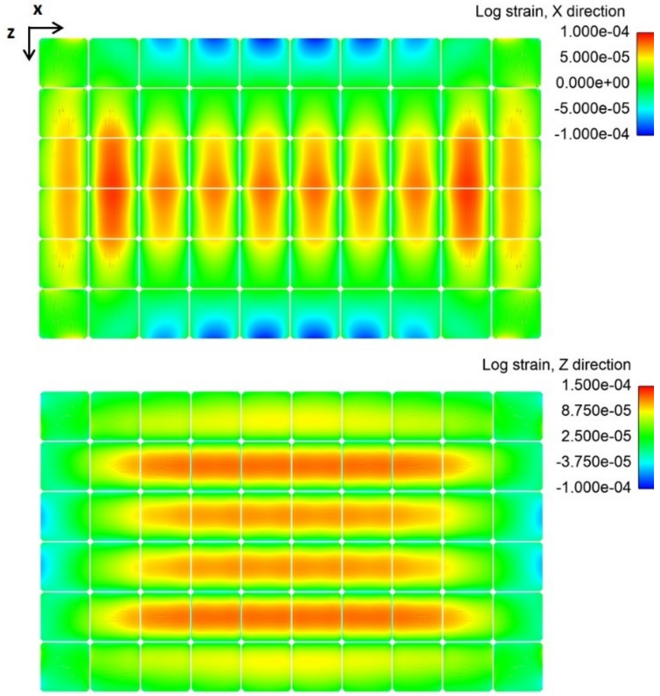

Figure 2-4: Predicted strain map for instrumented photovoltaic modules.

2.3. Module fabrication process

Modules were constructed by D2Solar LLC on commercially representative process equipment. Cells were interconnected on an automated stringer, and layup was performed manually onto the glass and front encapsulant sheets. Gauge adhesion and wire soldering were conducted in-situ on the cell layup, and wire routing was facilitated with PET alignment tape. Wires and cell tabbing were routed through the rear encapsulant and backsheet sheets during final assembly. The construction process is shown in Figure 2-5 to Figure 2-7, and the lamination processing conditions are shown in Figure 2-8.

Figure 2-5: Layup of interconnected photovoltaic cells onto glass and front encapsulant.

Figure 2-6: Electrical connections between photovoltaic cell rows and tabbing of connections to be fed into module junction box.

Figure 2-7: Rolling of EVA sheet over photovoltaic cells (left) and the placement of the back layer on top of the module (right).

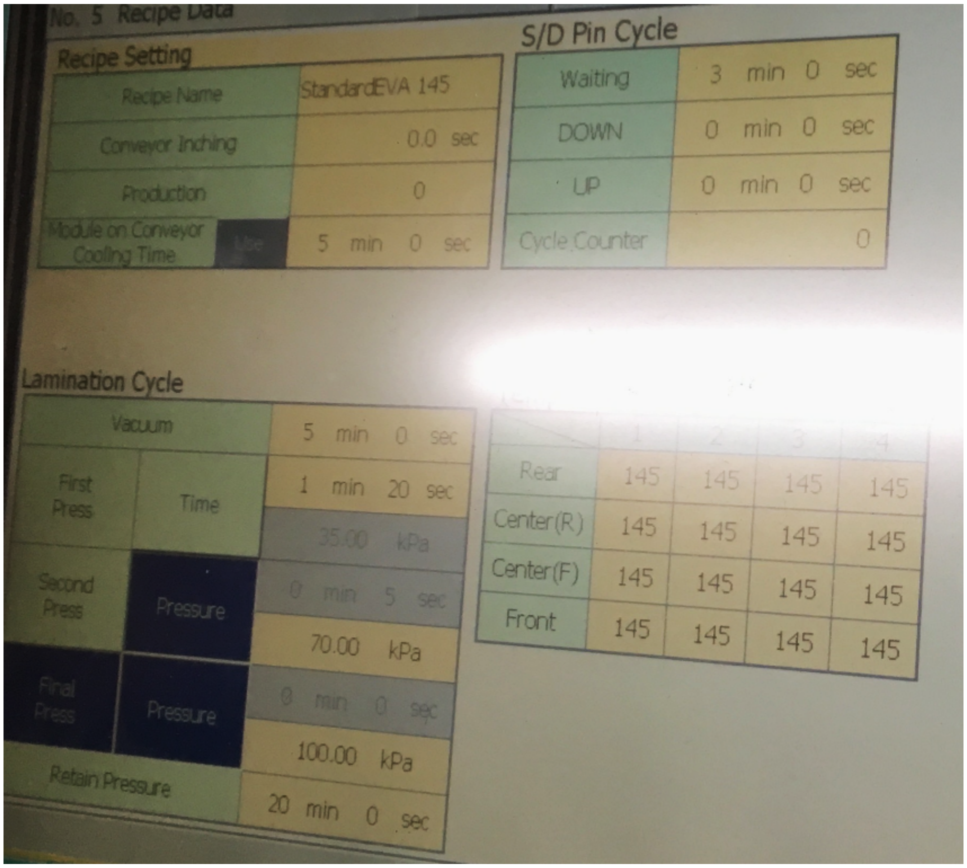

No. 5 Recipe Data

Recipe Setting

Recipe Name		StandardEVA 145
Conveyor Inching		0.0 sec
Production		0
Module on Conveyor Cooling Time	Use	5 min 0 sec

S/D Pin Cycle

Waiting	3 min 0 sec
DOWN	0 min 0 sec
UP	0 min 0 sec
Cycle Counter	0

Lamination Cycle

Vacuum		5 min 0 sec
First Press	Time	1 min 20 sec
		35.00 kPa
Second Press	Pressure	0 min 5 sec
		70.00 kPa
Final Press	Pressure	0 min 0 sec
		100.00 kPa
Retain Pressure		20 min 0 sec

	1	2	3	4
Rear	145	145	145	145
Center(R)	145	145	145	145
Center(F)	145	145	145	145
Front	145	145	145	145

Figure 2-8: Module lamination process conditions.

2.3.1. *Test coupons*

Prior to module fabrication, single cell coupons were produced with strain gauges of the same types to be used attached in the same configurations specified for the full modules. The same materials to be used in actual modules were used for the coupon laminates. The gauges and cells in these coupons were electrically functional, and the strain measurement concept was successfully demonstrated in an ad-hoc 4-point bending test. Coupons were retained and are available for additional small-scale testing and gauge output validation.

2.3.2. *Fabrication lessons learned*

Some lessons learned between the test coupon and actual module builds include:

1. Gauge wire selection and density: 30-gauge, polyimide-insulated, solid strand copper wire was selected for gauge connections [8]. These were amenable to lamination processes, with no observed bubbles or cell cracking near wire bundles, even with minimal organization and up to 3 stacked wire intersections (Figure 2-9). Cracks were present when 4+ simultaneous wire intersections occurred. This suggests that good workmanship is ideal but with some available margin for error or additional instrumentation density. Insulation integrity appeared to be maintained without issue and no failures occurred during handling.

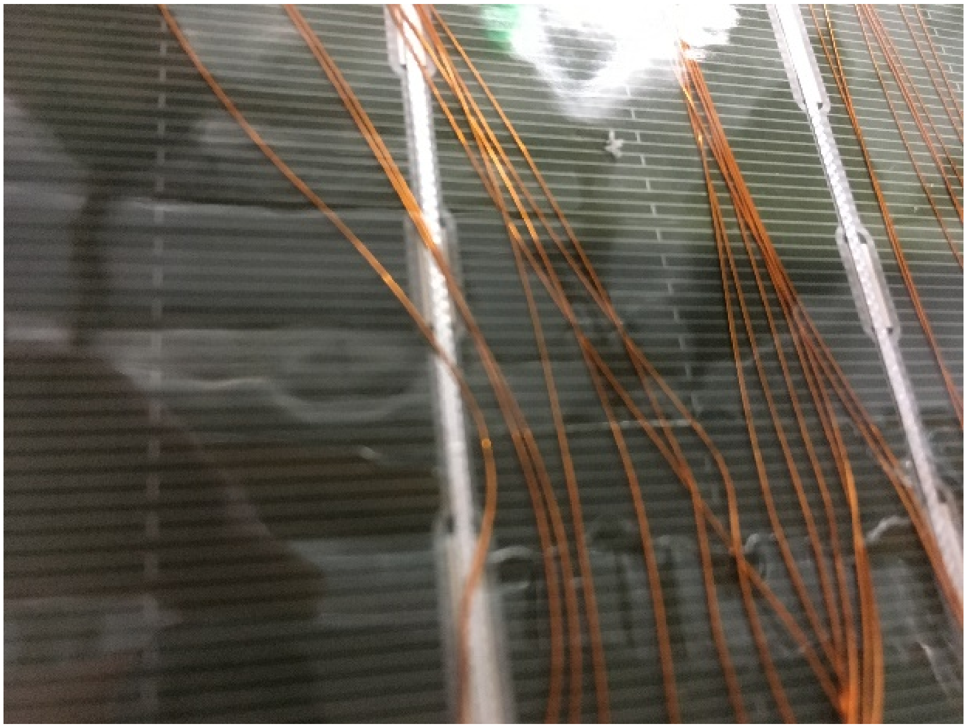

Figure 2-9: Intersections of copper wires during lamination. No cell cracking or bubbles were observed.

2. Alignment tape: Both Kapton and PET tape were used within coupons to provide wire management. PET tape was found to laminate seamlessly and was preferable, since Kapton tape had small bubbles present.
3. Gauge soldering: Solder paste was found to be helpful for forming gauge connections, rather than wire solder. If available, pre-soldered gauges would be preferable, due to the extremely thin package and the need to work directly on fragile silicon cells and heat-sensitive encapsulant sheets

2.4. Pretest characterization

Gauge continuity was confirmed for all modules, with 1 failure (open circuit) detected among the 40 implemented gauges (80 total wire connections). The cause was not found definitively but could have been due to mediocre soldering to gauges or a hidden wire break. Characterization by electroluminescence (EL) imaging was also performed, with no cell cracks detected. Significant cell mismatch was observed but was not of concern since no electrical quality standards were specified. Nonetheless, a lesson learned could be to still impose a minimal cell binning criterion, to improve EL image contrast without requiring additional processing.

3. TESTER AND DATA ACQUISTION HARDWARE

3.1. LoadSpot Mechanical Module Tester

Mechanical tests were performed on the LoadSpot module mechanical tester [6]. This air pressure-based tester imposes a mechanical load via vacuum or positive pressure behind the module, while sealed to a rigid test cavity along its frame (Figure 3-1 to Figure 3-3). Since the full module face was accessible, simultaneous EL imaging was performed. Additionally, 9 optical deflection measurements on the module back side were made using built-in sensors. Test sequences (pressure load set point, EL image acquisition, deflection measurement acquisition vs. time) was directly programmed to synchronize operation with clock time.

Figure 3-1: Backside of test environment showing center vaccum port.

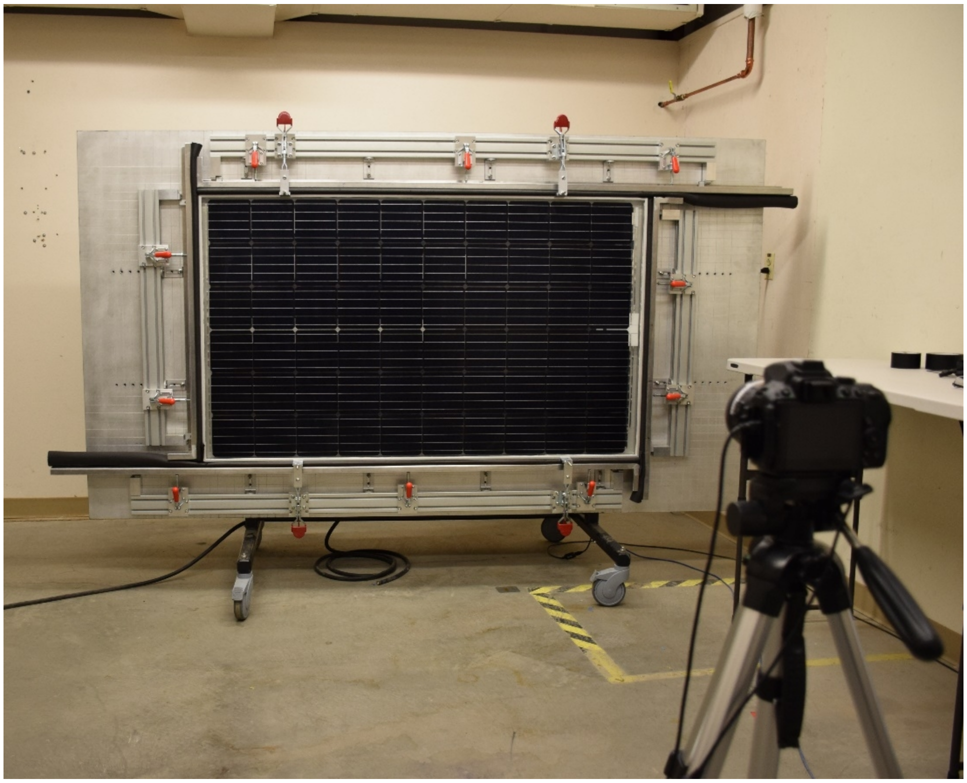

Figure 3-2: Front side of test environment with module secured via four clamps (two top and two bottom) and sealed to a rigid test cavity along its frame. Camera shown is for EL imaging.

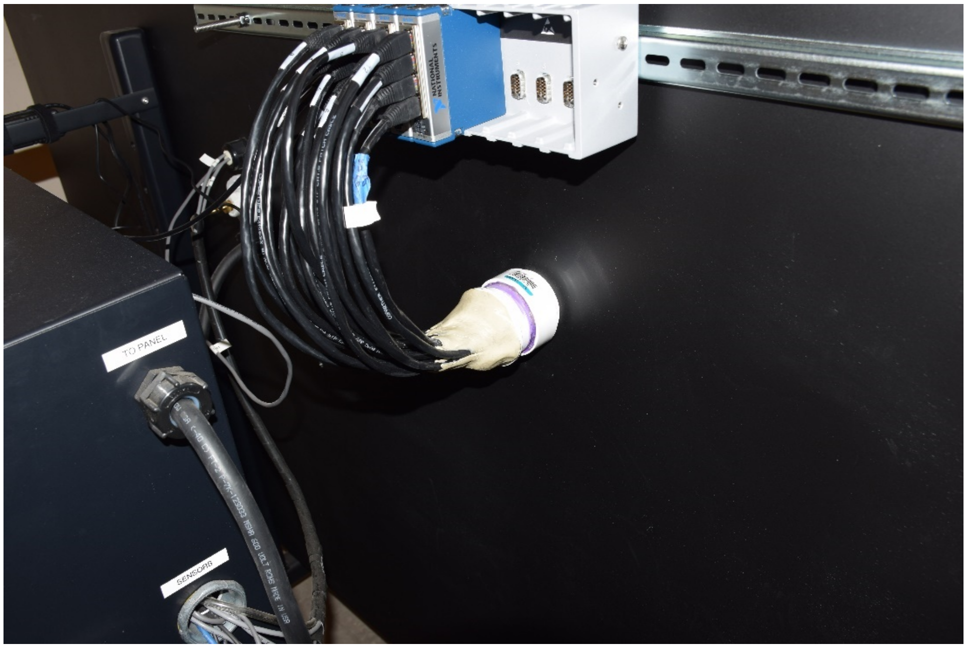

Figure 3-3: Backside of test environment showing cables used for sensor data retrieval and associated hardware mounting.

3.2. Strain gauge data acquisition

Strain gauge leads exiting the module were first routed to a terminal block on the junction box, to secure and organize the many small wires. A National Instruments interface was then implemented on the LoadSpot itself, beginning with a connector block to mate with the terminal block on the instrumented modules and transfer gauge outputs through paired cables. NI9237 plug heads containing a built-in Wheatstone bridge [9] were used to receive and amplify strain gauge output from the paired cable wires. Output signals were sent via RJ45 cables outside of the LoadSpot to NI9949 card readers. Output from card readers was sent to a laptop via a standard USB interface, and interpreted in a LabView executable. Since the laptop also controlled LoadSpot operation and data acquisition, data files were synchronized based on the common system timestamp.

3.3. Mechanical test cycles

Test cycles are summarized in Table 2 and Table 3 along with data acquisition types and intervals for each. Separate "safe" and "full" test cycles were defined, with the goal of the "safe" cycle being to test seals and acquire an initial, repeatable data set without causing module damage. If successful, the "full" cycle was then run to collect remaining data objectives.

Table 2: "Safe" Test Cycle and Collected Data Quantities

Load Recipe	EL imaging	Strain data	IR deflection
0 to -1000 to 0 Pa, 100 Pa increments. Hold for 20 minutes at -1000 Pa	Every 100 Pa, and after 20-minute hold at -1000 Pa	Continuous (1Hz)	Continuous (1Hz) except during EL

Table 3: "Full" Test Cycle and Collected Data Quantities

Load Recipe	EL imaging	Strain data	IR deflection
0 to -2400 to 0 Pa, 100 Pa increments. Hold for 20 minutes at -1000 Pa and again at -2400 Pa	Every 100 Pa, and after 20-minute holds at -1000 Pa and -2400 Pa	Continuous (1Hz)	Continuous (1Hz) except during EL

4. SIMULATION MODELS

A finite-element analysis of the photovoltaic module provides the expected strain and displacement fields within the module during the mechanical testing procedure. In isolation, conducting a finite-element analysis is not sufficient to predict with confidence the response of a structure subjected to external forces; experimental measurements must be obtained to validate the model. The experimental measurements available to validate computational simulations have been restricted to external values, like discrete displacements on accessible surfaces. Validating a finite-element model against direct strain measurements obtained by strain gauges in a testing environment will lead to further understandings of damage and degradation mechanisms of photovoltaic modules in the field.

4.1. Finite-Element Model

The objective of developing a finite-element model was to represent both the photovoltaic module and the testing conditions accurately, so the mechanical response could be validated against experimental measurements. The main characteristics we considered were the module geometry, material properties, test-fixture boundary conditions, material interactions, applied loading profile, and sensor locations.

4.1.1. Module design

First, we attempted to represent the physical module in Cubit [10]. A standard ACIS Text (.sat) file of a similar photovoltaic module used in a previous simulation was modified to conform to the specified geometry of the current module [1,5]. Since the photovoltaic module design is symmetric with respect to its width and length, we used quarter-symmetry to achieve a higher fidelity model with reduced computational cost. It is important to note that the use of symmetry is valid only if the applied loading is also symmetric.

We referred to Figure 2-1 to determine the measurements of the aluminum frame cross-section. We did not have exact measurements for all quantities of the extruded aluminum, but we knew the height was 45 mm and the width was 35 mm, as stated previously. Normalizing the number of pixels along the length and width of Figure 4-1, the other measurements were also determined. The progression of the old-to-modified cross section is given in Figure 4-2 and the comparison between it and the physical module are summarized in Table 4.

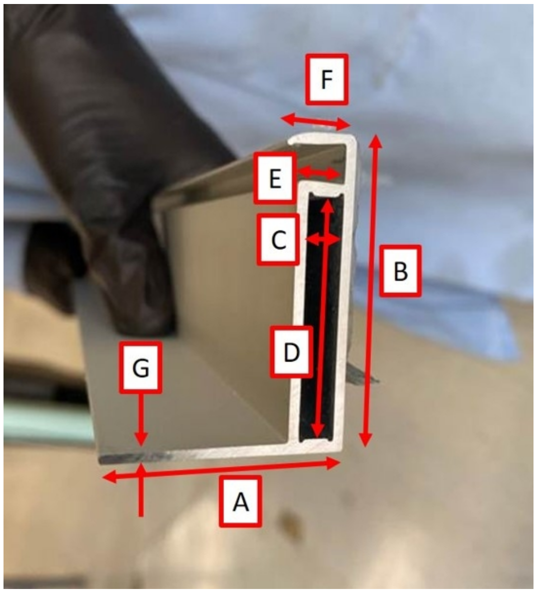

Figure 4-1. Labeled frame cross-section to determine dimensions. Edges 'A' and 'B' known to be 35 and 45 mm, respectively.

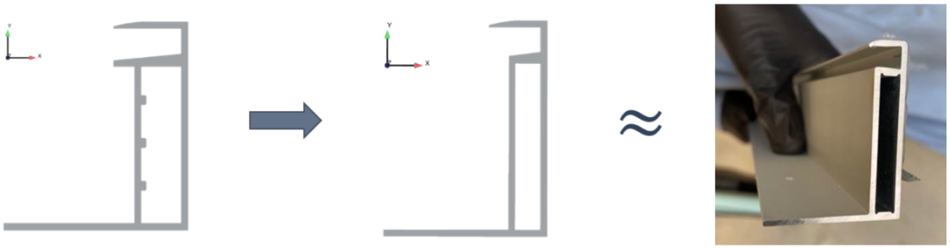

Figure 4-2: Progression of frame cross-sections from original model to updated module, compared to actual frame.

Table 4: Geometric measurements of physical module and simulation model

Location	Physical Module (mm)	Simulation Model (mm)	% Error
A	35.00	34.31	1.97
B	45.00	45.38	0.84
C	5.22	5.22	0.00
D	34.68	34.78	0.29
E	6.30	8.12	28.89
F	8.14	12.32	51.35
G	1.37	1.49	8.76

From Table 4, the geometry was represented accurately except for locations E and F—the upper and lower flanges used to secure the module. Significant modifying of features would have been required to adjust locations E and F, which was expected to take too much time repairing the Cubit meshing journal file. Since the module did not contact the overhang at location F, it was deemed unlikely to cause noticeable discrepancies in either the displacements or strains of the cells. However, the errors in second moment of area between the simulation and physical frames are 22.2% about the horizontal axis and 3.2% about the vertical axis. This error was not calculated before running the simulation. By reducing the length of F from 12.32 mm to 8.12 mm (the most time-efficient length reduction), the errors in the second moment of area reduces from 22.2% to 11.5% and from 3.2% to 2.9%. The remaining error is attributed to the difference in thickness (location G). The new value of F will be used in future simulations.

Next, the module layup and dimensions were modified to represent the physical module, as seen in Figure 2-2. The bottom of the module was the PET backsheet. Above the backsheet was the grid of equidistant solar cells surrounded by the EVA encapsulant. Resting on top was the glass section with thickness 2.8 mm, matching the thickness of the physical module. The top of the glass surface was subjected to the pressure loading to simulate the testing environment of the physical module.

The module was inserted into and secured to the frame grooves with silicone sealant, shown in Figure 4-3. The sealant thickness was chosen such that the module is centered in the frame.

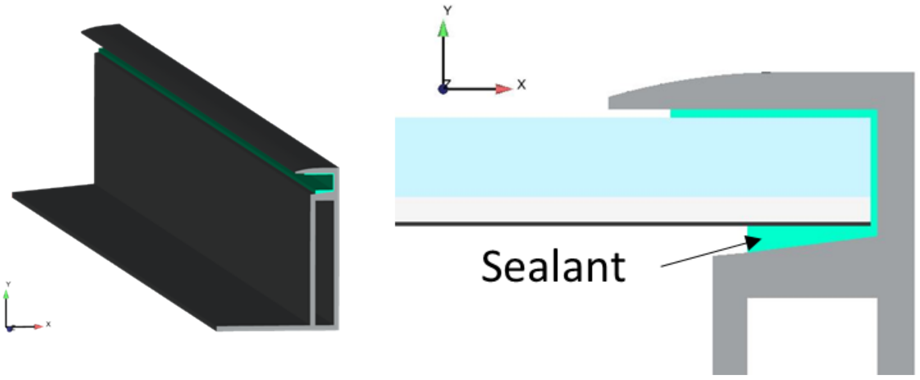

Figure 4-3. Views of the frame and the mated module and frame, with edge sealant labeled.

A difficulty of modeling real systems is representing the boundary conditions accurately. From Figure 3-2, the frame was secured to the test fixture by four supports (two along each long edge). We attempted to represent these conditions by bolting the frame flange to a fixed support structure, as seen in Figure 4-4.

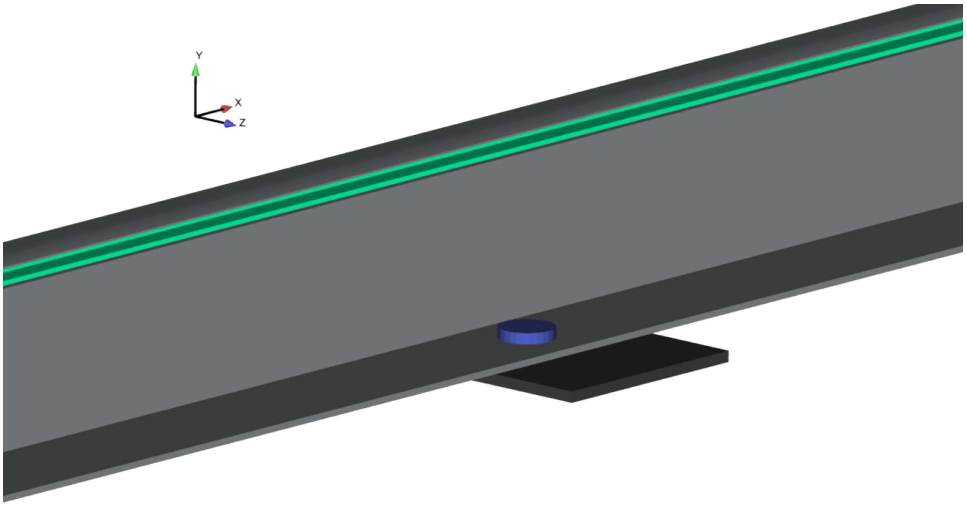

Figure 4-4: View of module frame and bolted support.

This representation was not perfect. In Figure 3-2, the placement of the clamps in the test fixture was not exactly symmetric; accounting for this asymmetry would require a full-sized model at larger computational cost. Additionally, the force required by the bolt head to secure the frame in Figure 3-2 was not known. A force of 1555 N was applied in the model, estimated from the manufacturer recommended fastening torque converted to a normal force. Although some inconsistencies remained, the simulated module boundary conditions were the best available representation of the physical module and sufficient for the purposes of this study.

The last geometric consideration was the corner key, as seen in Figure 4-5. In the physical module, the aluminum corner key was press-fit into the aluminum frames, held in place by contact forces. In the simulation, we represented this interaction by inserting the key into the two frame sections with zero gap and defining a friction coefficient of 1.15 between the aluminum key and aluminum frame surfaces.

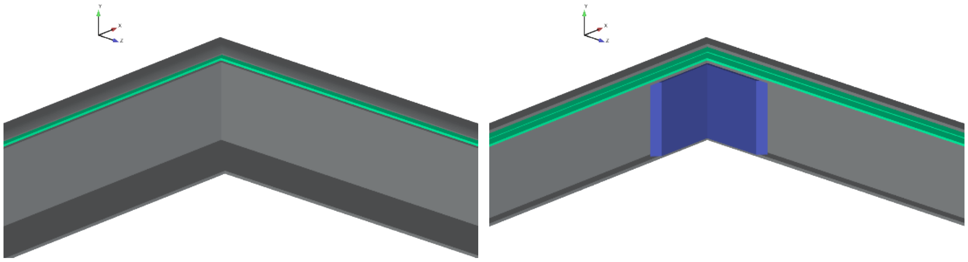

Figure 4-5. Cutaway view of aluminum corner key inside the frame sections.

The whole module, as mentioned in Section 2, was 1656 mm wide and 991 mm long. Thus, the quarter-symmetric module needed only to be 828 mm by 495.5 mm. The full assembly is shown in Figure 4-6.

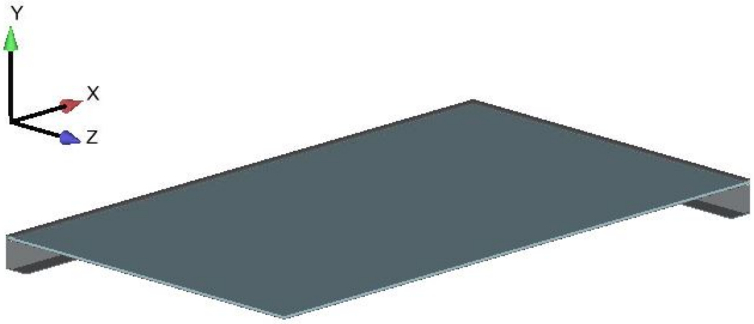

Figure 4-6. Full view of the quarter-symmetric photovoltaic module

By mirroring Figure 4-6 about its two planes of symmetry and making the glass and encapsulant semi-transparent, we can see all 60 cells of the full module shown in Figure 4-7, which is representative of the tested physical module architecture.

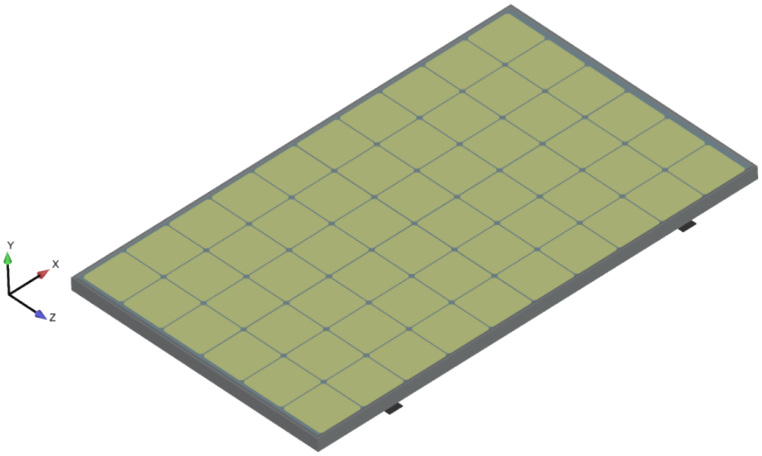

Figure 4-7. Representation of whole photovoltaic module mirrored about symmetric planes and with semi-transparent glass and encapsulant components.

4.1.2. *Module materials*

The material selection was also an important consideration for representing the physical module accurately. Table 5 lists the mechanical properties for all module components that were modeled as elastic materials. These properties were carried over from parametric simulations conducted on similar modules with an identical bill of materials [5].

Table 5: Material selection for each module component

Component	Material	Density (kg/m^3)	Young's Modulus (GPa)	Poisson ratio
Frame & Corner Key	Aluminum	2700	67	0.315
Sealant	Adhesive	1300	0.00076	0.320
Glass	Glass	2500	71	0.253
Backsheet	PET	1500	3.0	0.496
Cells	Silicon	2300	170	0.292
Bolt Head & Support	Steel	7800	190	0.289

The module component left out of the above table is the encapsulant, which surrounds the silicon cells. Often the encapsulant is modeled as an elastic solid for computational cost considerations. The photovoltaic community, however, has recognized the importance of capturing the viscoelastic behavior of the encapsulant [2]. Thus, we decided to model the section as a viscoelastic material for increased fidelity.

In the literature, a viscoelastic material model for EVA was published [2], which characterized the time-dependent relaxation behavior by a high-fidelity 44-term Prony series and the temperature-dependent behavior by the William-Landel-Ferry (WLF) parameters. The shear modulus behavior, G, is described by a generalized Maxwell model, given by

$$G(t,\theta) = G_\infty + (G_0 - G_\infty)\sum_{n=1}^{N} g_n \exp\left(-\frac{t}{\tau_n}\right); \quad \sum_{n=1}^{N} g_n = 1\#(1)$$

with time-temperature dependence

$$G(t,\theta) = G\left(t^*,\theta_{ref}\right) = G\left(\frac{t}{a(\theta)},\theta_{ref}\right)\#(2)$$

where G_0 is the instantaneous shear modulus, G_∞ is the long-term shear modulus, τ_n are the Prony series time constants, g_n are the Prony series shear coefficients normalized by G_0, t is real time, θ is temperature, and t^* is the temperature-shifted time according to the shift function $a(\theta)$ compared to some reference temperature θ_{ref}.

The above time-dependent representation of the shear modulus is implemented in the Universal Polymer Model (UPM) in the SIERRA Adagio module; however, the UPM limits the user-input to only thirty Prony series terms. Thus, we obtained a lower-fidelity, 22-term Prony series description of the EVA time-dependent behavior [11]. Table 6 gives the values of the time-independent properties; the time-dependent Prony series coefficients are listed in Appendix B.2.

Table 6: Time-independent properties for EVA

Property	Value	Units
Density (ρ)	931	kg/m^3
Bulk Modulus (K)	30.7	GPa
Instantaneous Shear Modulus (G_0)	619	MPa
Long-term Shear Modulus (G_∞)	0.521	MPa

The WLF equation, to which the parameters given in [2] pertain, is

$$\log a_T = \frac{C_1\left(\theta - \theta_{ref}\right)}{C_2 + \left(\theta - \theta_{ref}\right)} \#(3)$$

where C_1 and C_2 are fitting parameters used to construct the master curve and a_T is the horizontal shift value. The equation exploits the time-temperature superposition principle of linear viscoelasticity. The WLF parameters for EVA from [2] are provided in Table 7.

Table 7: WLF parameters for EVA

Property	Value	Units
Reference Temperature (θ_{ref})	243	K
WLF C_1	645.99	-
WLF C_2	2122.36	K

Before implementing the viscoelastic material model into the module simulation, the material model was validated against experimental results. By doing so, we could confirm that the low-fidelity, 22-term Prony series could capture the stress relaxation behavior observed in [2]. The results show good agreement, as discussed in Appendix B.3, which suggests that the material model was implemented correctly and could be used confidently in the full module simulation.

4.1.3. Module discretization

After constructing the module geometry, as shown in Figure 4-6, the module needed to be discretized for use in the finite-element simulation. An existing Cubit journal file, which was used to create the mesh of the previous module, was adapted to discretize the current module [5]. Modifications were made to account for the removed features, i.e., the three internal ribs within the web (Figure 4-2), and for the slight changes in length, width, and height of each component.

The completed mesh used 3.2 million uniform gradient Hex8 elements (eight-node hexahedron elements). To judge the quality of the mesh, the shape metric was evaluated for all elements, grouped by module section. A shape metric of unity indicates a perfect, cubical element; a value approaching zero indicates a severely skewed element (i.e., the width and length may be far larger than the thickness). It is customary to keep the shape metric of all elements above 0.20 to ensure convergence of finite-element simulations and to prevent elements from inverting [12]. Table 8 lists the minimum and average shape metric for each section of the module.

Table 8: Mesh summary for photovoltaic module

Section	Number of Elements	Minimum Shape Metric	Average Shape Metric
Backsheet	353804	0.1069	0.1991
Bolt Head	267	0.2308	0.6483
Corner Key	4301	0.3305	0.8259
Glass	884510	0.4295	0.7650
Frame	310149	0.1565	0.5730
Sealants	39838	0.1102	0.2826
Support	3684	0.2615	0.9319
Encapsulant	1121658	0.1180	0.2852
Cells	470460	0.1467	0.1852
Total Model	**3188671**		

The silicon cells and the PET backsheet proved to be the most difficult elements to maintain an adequate average shape metric, given that they are the thinnest sections. Increasing the number of elements through the length and width of these sections would improve the shape metric but would increase the number of elements greatly since it would influence the mesh of adjacent sections. For example, doubling the number of elements along the length and width of the backsheet would improve the average shape metric by about four times and would increase the number of elements from 350,000 to 1,400,000; however, doing so would also refine the mesh of the glass, frame, sealant, encapsulant, and cells, which could increase the total number elements by a factor of four. Thus, to balance computational cost with accuracy, a lower-bound on the shape metric of 0.10 was maintained. Although marginal, this quality was found to be useable for mechanical loading simulations where deflections were small and primarily in-plane. A mesh convergence study could be conducted in future work to verify that the minimum shape metric is sufficient.

4.2. Testing configuration

The final considerations before running the simulation were the applied loading profile imposed by the vacuum and the locations of the displacement and strain readings.

4.2.1. Simulation loading profile

The four modules were all tested with the same loading profile, as outlined in the load recipe of Table 3. Ideally, the elapsed time versus applied load of the module would be identical; however, as shown in Figure 4-8, small offsets could be seen since the LoadSpot tester was operated to ensure fixed hold times at each pressure setpoint so transient control times varied. Since the loading time of the four modules were reasonably close, the loading profile used for the simulation was then taken to be the average of the four module pressure profiles, also shown in Figure 4-8.

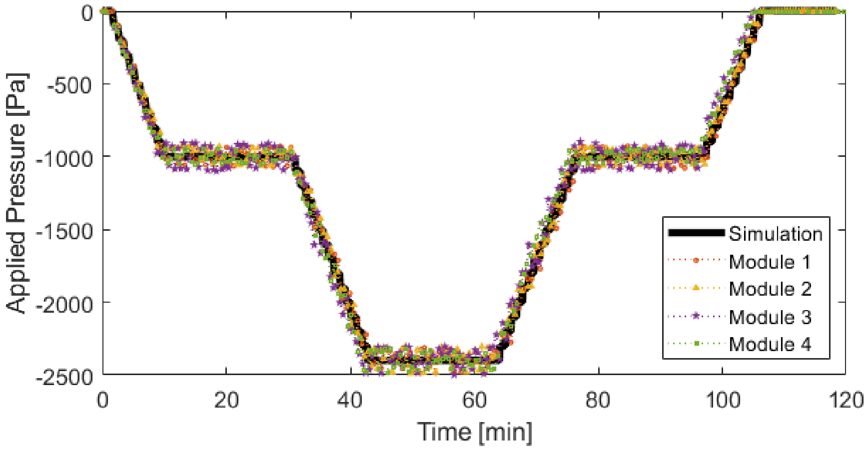

Figure 4-8: Pressure loading profiles as measured in the LoadSpot cavity of the four modules and the simulation.

The vacuum in the test environment, on the back side of the module, creates a pressure gradient, which results in a positive pressure against the front side of the module. The absolute value of the pressure profile in Figure 4-8 was applied uniformly to the front face of the module glass.

4.2.2. *Output requests*

Output files were generated for the simulation: two for the module displacements, two each for the strain locations associated with Modules 2, 3, and 4, as given in Figure 2-3. The displacements obtained by the simulation are recorded as the nodal displacements at locations nearest to the optical sensor locations as shown in Figure 4-9. The strains are taken to be the strains at elements nearest to the locations as presented in Figure 2-3.

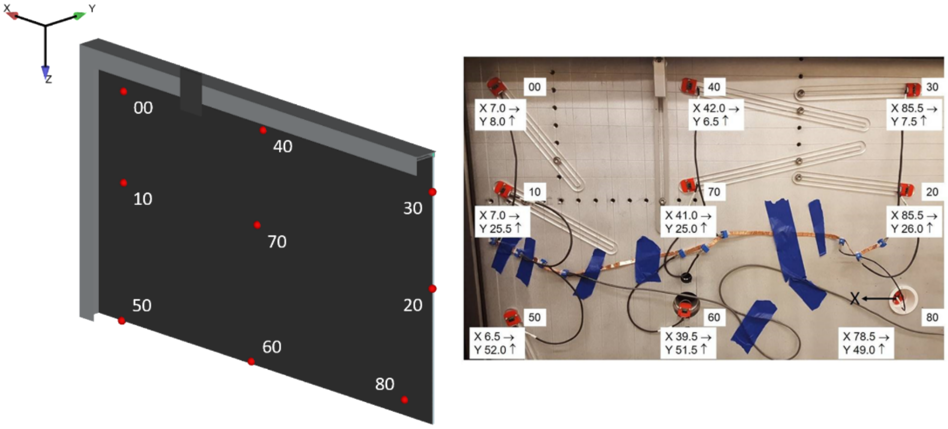

Figure 4-9: (Left) Nodal displacement locations. Y-deflection is output on the surface of the backsheet. (Right) Optical sensor locations annotated with (X,Y) coordinates and label. Note: Simulation and annotated experimental coordinate systems have transformed axes.

5. RESULTS AND DISCUSSION

The simulation of the quarter-symmetry photovoltaic module with a viscoelastic EVA encapsulant was conducted using the TLCC2 HPC platform at Sandia National Laboratories; it required two weeks to complete on 480 processors, at 2.6 Ghz with 4-GB RAM available per processor.

5.1. Displacement measurements

First, a contour plot of the glass displacement field at the peak load of 2400 Pa is presented in Figure 5-1 to provide a qualitative check of the simulated pressure application on the module.

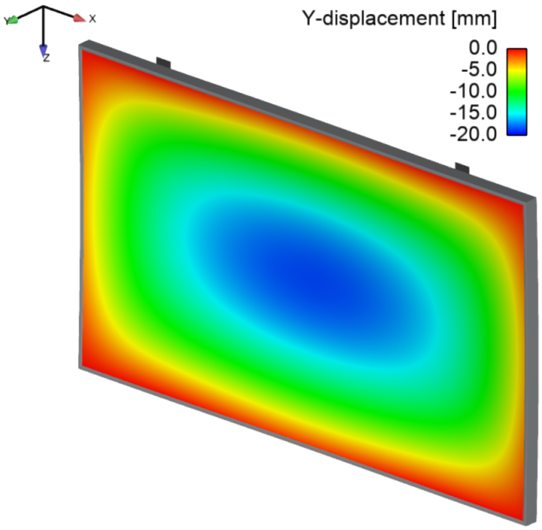

Figure 5-1. Contour of displacement field at pressure 2400 Pa.

The center of the module deflects in the direction of the pressure gradient. The edges of the glass in-line with the clamps on the long side of the module (x-direction) undergo almost no deflection; the glass midway along the edge on the short side of the module (z-direction) exhibits a small displacement since it is not supported directly, resembling the bending of a beam. We can see this same behavior in the physical module, shown in Figure 5-2.

Figure 5-2: Deflection of physical module under applied pressure.

To provide a quantitative comparison of these displacements, the optical sensor data can be analyzed concisely along a diagonal path from the corner (sensor "00") to the center (sensor "80") of the module, as represented in Figure 5-3. Module displacements are measurable optically as a decrease from the initial sensor-to-module-backsheet distance, as the module displaces inward toward the sensors under vacuum (net external pressure).

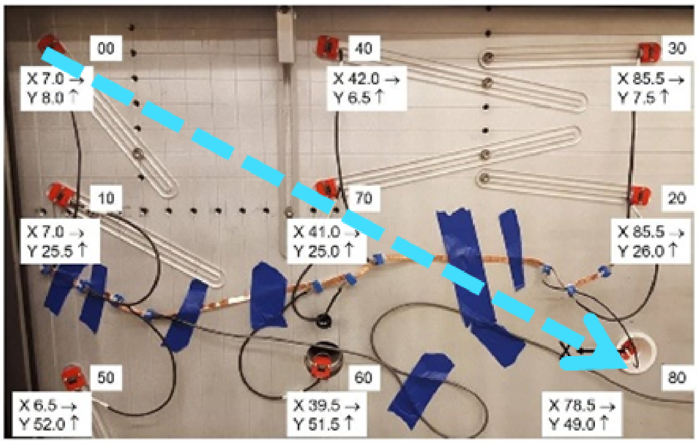

Figure 5-3: Path of interest on the quarter panel to compare displacements from experiment and simulation. Module center located at approximately position 80.

The resulting displacements from the three sensors along the above path can then be compared between the simulation and the four module experiments. Figure 5-4 to Figure 5-6 show the displacements for the three sensors that fall along this path at the five discrete pressures, 0 Pa, 1000 Pa, 2400 Pa, 1000R Pa, and 0R Pa, where "R" indicates the hold period after returning from the peak load. Since the displacement changed over the twenty-minute period that each pressure was applied, the average displacement within the first and last ten seconds of the pressure-hold period was used.

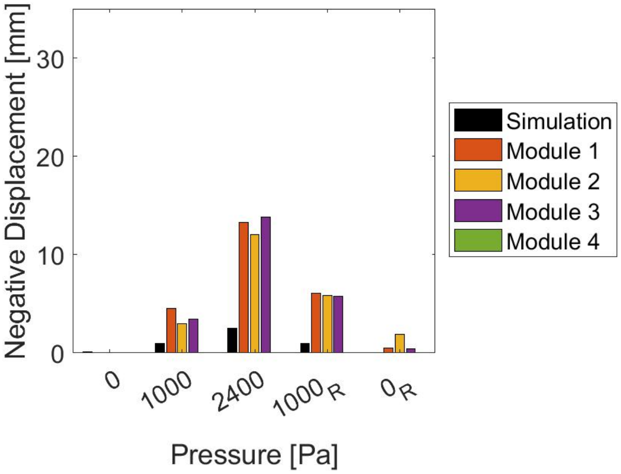

Figure 5-4: Displacement averages at sensor 00, nearest to the module corner.

At 0 Pa pressure in Figure 5-4, no displacement is predicted, as expected. Increasing the pressure to 1000 Pa and again to 2400 Pa increases the displacement predicted by the simulation and measured in three of the modules. It was noticed after the conducting the experiment on Module 4 that sensor 00 was not operating, so no displacements were obtained for Module 4. The remaining three modules show moderate variability in the measured displacement. It is clear, however, that the simulation underpredicted the displacement by approximately 3-5 mm at 1000 Pa and 1000R Pa, and by 10 mm at the peak pressure.

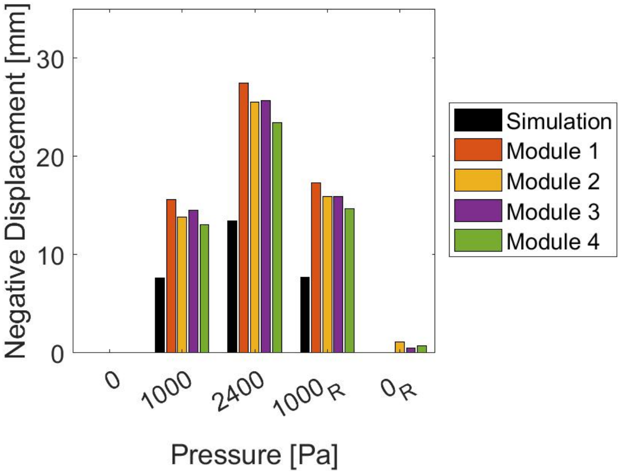

Figure 5-5: Displacement averages at sensor 70, midway between module corner and center.

At sensor 70, the displacements summarized in Figure 5-5 are larger in magnitude than those at sensor 00. In this case, sensor 70 was operating during all four module tests. The displacement of the four modules is in agreement, with a maximum relative error of only 5% at 2400 Pa. Again, the simulation underpredicted the displacement at this sensor location by nearly a factor of two. It is also interesting to note that at the end of the test (pressure 0R Pa), the measured displacement did not read zero, suggesting that some path-dependent behavior was present.

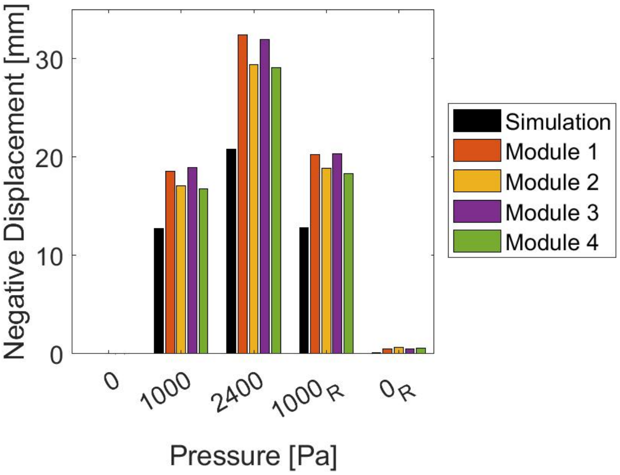

Figure 5-6: Displacement averages at sensor 80, center of module.

The displacements at the center of the module shown in Figure 5-6 follow a similar trend as the previous sensor locations, although the relative error between the simulation and experiments is less. As predicted by the contour plot in Figure 5-1, the displacement at the sensor nearest to the corner is the smallest in magnitude; whereas, the maximum displacement is attained at the center.

To investigate the relaxation behavior of the modules during the twenty-minute periods where the pressure is held constant, we plot the average displacements of all modules versus the elapsed time for the three nonzero discrete pressures, as shown in Figure 5-7 to Figure 5-15. The mean response for each sensor was taken as average displacement of four modules (three, in the case of sensor 00). The 2σ bounds in Figure 5-7 to Figure 5-15 were then constructed by computing the standard deviation of the module measurements and centering the bounds around the sensor mean. For completeness, the data for all sensor locations are included.

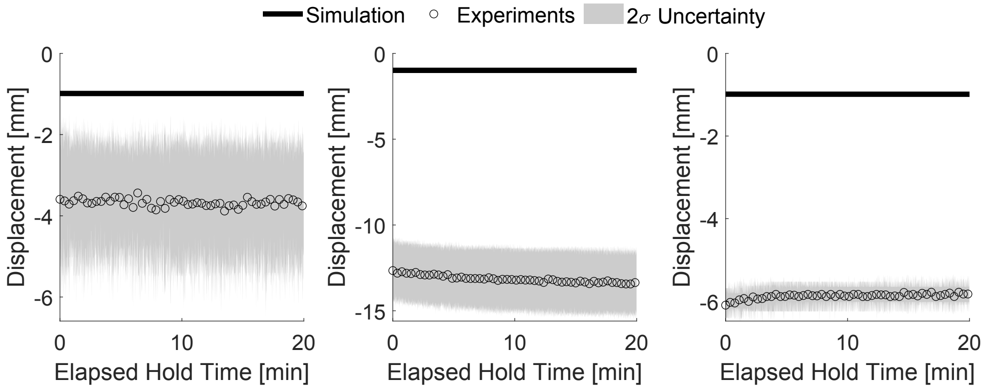

(a) Pressure = 1000 Pa **(b) Pressure = 2400 Pa** **(c) Pressure = 1000r Pa**

Figure 5-7: Displacement relaxation comparison at sensor 00 location. Experimental points taken as the average of the three modules. Recall: sensor 00 was not operating during the testing of Module 4.

The relaxation behavior at the corner sensor is negligible for the lower pressure holds, as shown in Figure 5-7 (a) and (c); about 1 mm of relaxation is observed while holding at 2400 Pa. Based on the difference in magnitude of the measured displacement in Figure 5-7 (a) and (c), there appears to be hysteresis in the deformation state, resulting possibly from either material or structural contributions; whereas, the simulated prediction shows nearly reversible deformations. The difference in magnitude between the simulation and averaged module data is comparable to the difference observed in the previous bar chart from Figure 5-4.

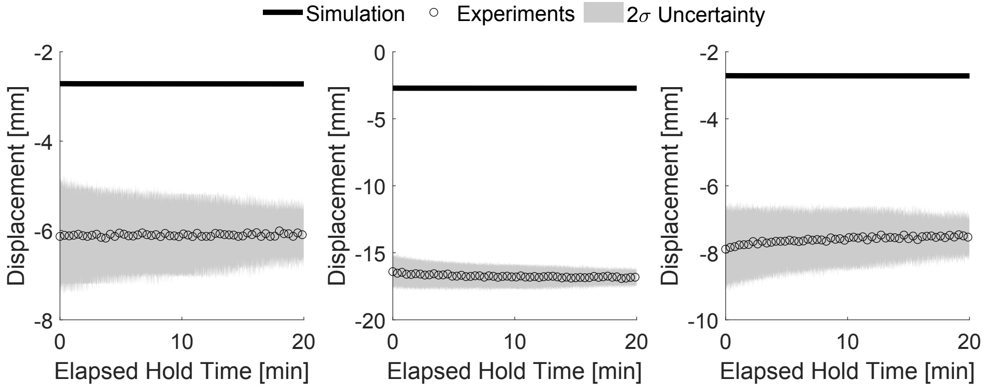

(a) Pressure = 1000 Pa **(b) Pressure = 2400 Pa** **(c) Pressure = 1000r Pa**

Figure 5-8: Displacement relaxation comparison at sensor 10 location. Experimental points taken as the average of the four modules.

At sensor 10, along the short edge, there is little relaxation behavior during any pressure-hold interval, as shown in Figure 5-8. The simulation predicts a difference of 0.02 mm in displacement between Figure 5-8 (a) and (c); whereas, the experimental average shows a difference of about 2 mm. The uncertainty in the measurements, shown as the shaded region, is no greater than 2 mm.

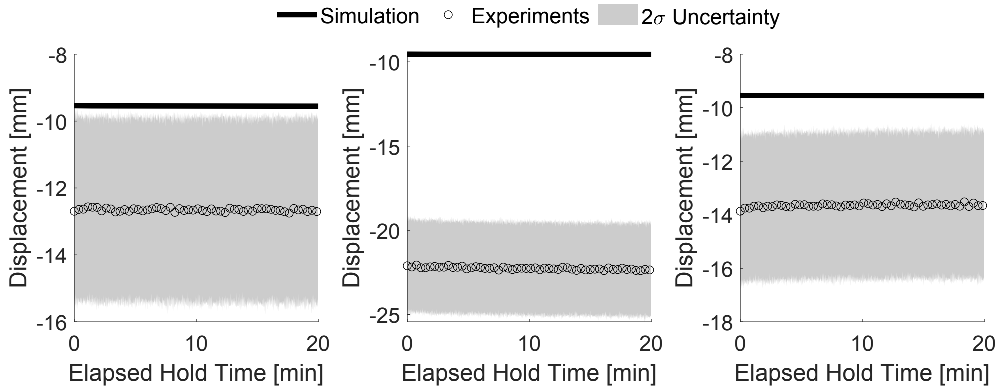

(a) Pressure = 1000 Pa **(b) Pressure = 2400 Pa** **(c) Pressure = 1000r Pa**

Figure 5-9: Displacement relaxation comparison at sensor 20 location. Experimental points taken as the average of the four modules.

Sensor 20 is located near the center of the module, as shown in Figure 5-3. Since it is closer to the center compared to sensors 00 and 10, the displacement magnitude is larger. The before mentioned trends of path-dependency, relaxation behaviors, and simulation-experimental comparisons in Figure 5-9 are unchanged from previous sensors. The uncertainty is within ±3 mm for all three pressure intervals.

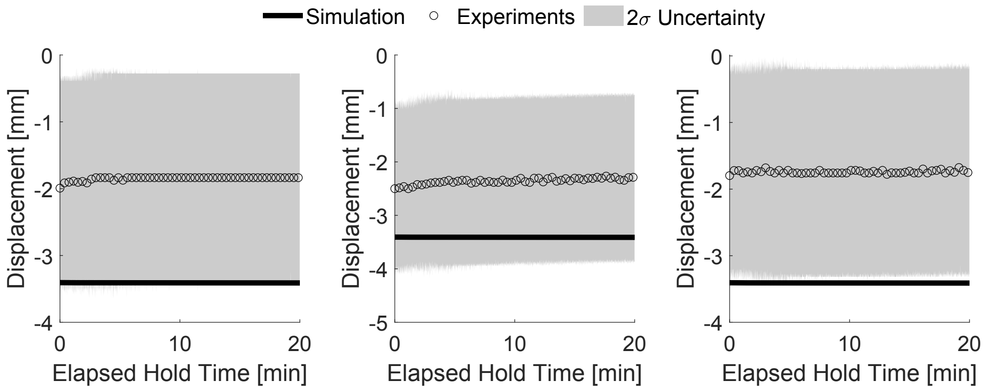

(a) Pressure = 1000 Pa **(b) Pressure = 2400 Pa** **(c) Pressure = 1000r Pa**

Figure 5-10: Displacement relaxation comparison at sensor 30 location. Experimental points taken as the average of the four modules.

The displacements at sensor 30 are the smallest compared to all other sensor locations. The relaxation behavior is minimal given the small displacement magnitude. This sensor is the only location where the displacement predicted by the simulation was greater than the measured displacement.

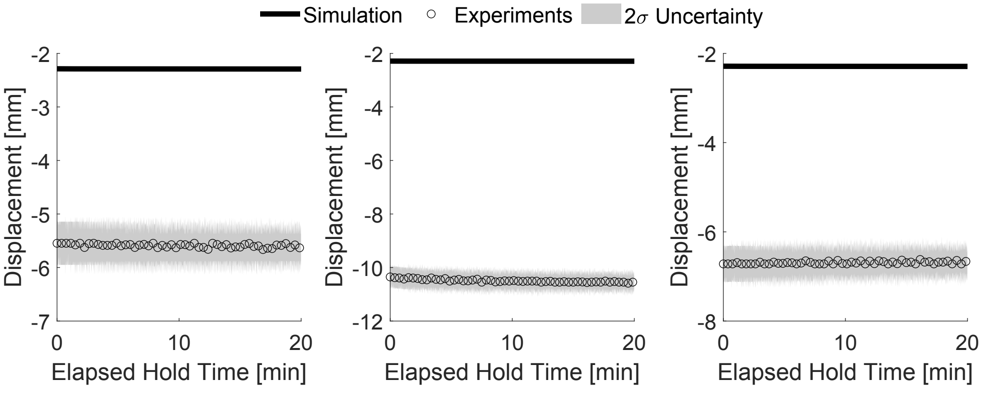

(a) Pressure = 1000 Pa **(b) Pressure = 2400 Pa** **(c) Pressure = 1000r Pa**

Figure 5-11: Displacement relaxation comparison at sensor 40 location. Experimental points taken as the average of the four modules.

Sensor 40, which is located along the long edge of the module, had measured displacements between two and three times greater than the predicted displacements. There is negligible relaxation at this location compared to the other locations.

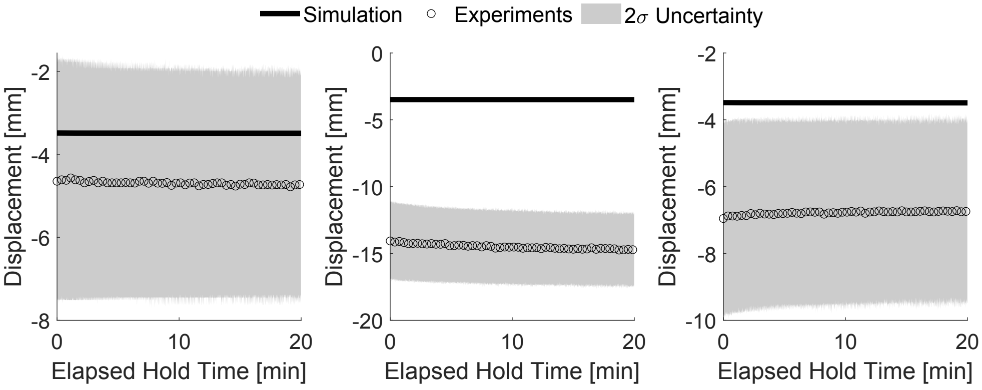

(a) Pressure = 1000 Pa **(b) Pressure = 2400 Pa** **(c) Pressure = 1000r Pa**

Figure 5-12: Displacement relaxation comparison at sensor 50 location. Experimental points taken as the average of the four modules.

Sensor 50 is located midway along the short edge of the module. The predicted displacement during the 1000 Pa pressure hold is comparable to the experimental values; however, when the pressure is increased to 2400 Pa the predicted displacement deviates more.

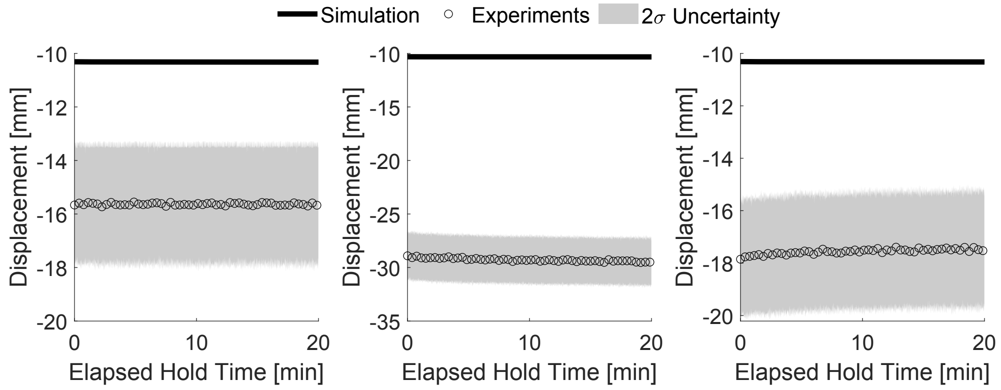

(a) Pressure = 1000 Pa **(b) Pressure = 2400 Pa** **(c) Pressure = 1000r Pa**

Figure 5-13: Displacement relaxation comparison at sensor 60 location. Experimental points taken as the average of the four modules.

Closer to the center of the module, sensor 60 displaced more than those near the edges. At 2400 Pa, the module relaxed by 2 mm over the 20-minute hold period, but the simulation still predicted no relaxation.

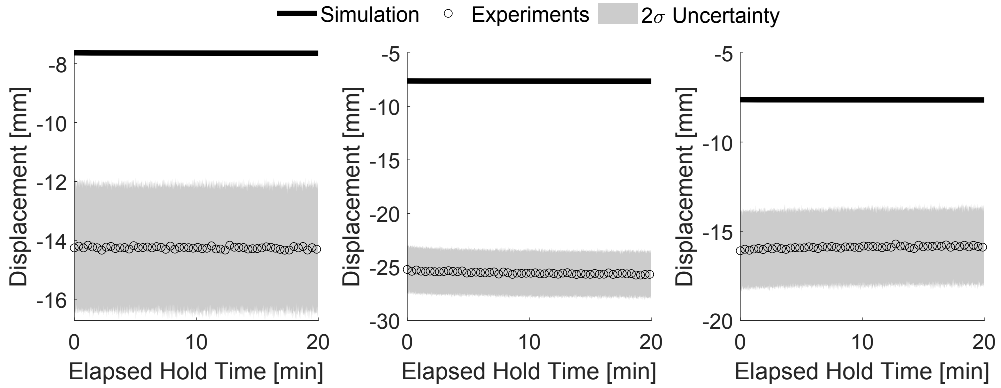

(a) Pressure = 1000 Pa **(b) Pressure = 2400 Pa** **(c) Pressure = 1000r Pa**

Figure 5-14: Displacement relaxation comparison at sensor 70 location. Experimental points taken as the average of the four modules.

As pictured in Figure 5-3 sensor 70 is along the diagonal. The magnitude of the displacement shown by Figure 5-14 is smaller than sensor 60 but follows a similar trend.

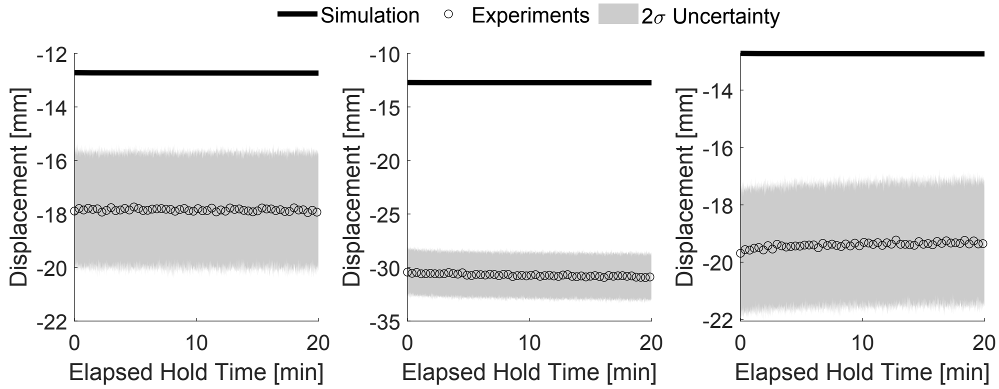

(a) Pressure = 1000 Pa **(b) Pressure = 2400 Pa** **(c) Pressure = 1000r Pa**

Figure 5-15: Displacement relaxation comparison at sensor 80 location. Experimental points taken as the average of the four modules.

Finally, the displacement at sensor 80 is largest in magnitude of any of the sensors since it is located in the center of the module. Even in this location, however, an average of only 0.45 mm of measured relaxation occurs across the 20-minute timespan at 2400 Pa; 0.015 mm of relaxation is predicted by the simulation.

We can conclude from the relaxation plots that the two-sigma uncertainties in the module experimental data are no greater than ±3 mm for any sensor or discrete pressure. It is also apparent from the results that there is no pronounced relaxation behavior in the simulated module. One explanation for this difference is the selection of encapsulant material, detailed in Appendix B.2, which was characterized for an EVA different than the one used in the physical modules. Another factor could be the idealization of other materials as elastic, such as the silicon edge sealant, when they should also be characterized as viscoelastic.

Finally, the magnitude of displacements predicted by the simulations differs from the average measured displacements by as much as ten times. In addition to the previously mentioned geometric errors summarized in Table 4, other inconsistencies between the simulated and physical PV modules, such as the corner key contact with the frame, the bolted constraint assumptions, and material property descriptions, may contribute to the observed difference in displacement magnitudes. It is possible that addressing these differences could reduce the displacement magnitude discrepancy between the simulation and experiments.

5.2. Strain measurements

To validate the accuracy of the *in-situ* strain measurements of the tested photovoltaic modules, we compare the measured strains to those predicted by the finite-element simulation. As described in Section 4.2.2, the simulated strains were computed for each sensor location of the physical modules. Since Module 1 was un-instrumented as a control, there are no strains to validate with simulation results.

Module 2 was fabricated to confirm that the module deforms symmetrically under the pressure loading. The strain gauge locations were depicted in Figure 2-3. Figure 5-16 and Figure 5-17 show the strain measurements in the x- and z-directions, respectively, for both the physical and simulated modules. In Figure 5-16, the gauges are grouped by color based on location: gauges 'A' and 'L' are symmetric pairs, as are 'B' and 'K', 'E' and 'H', and 'F' and 'G'. In Figure 5-17, all three gauges, 'C', 'I', and 'J', are located symmetrically.

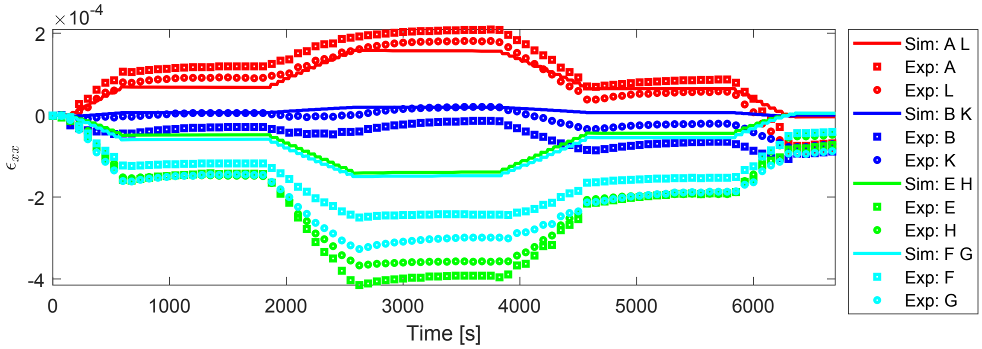

Figure 5-16: Comparison of strains in x-direction between simulation (Sim) and experiment (Exp) for each strain gauge in module 2.

The experimental measurements in Figure 5-16 show close agreement in x-strains between like gauge locations. The simulated strains at location 'A' and 'L' are nearly identical to the measured values. Based on the discussions in the previous section, this agreement is most likely attributed to the gauges being located along the module's edge. There is a larger difference in magnitude between the simulated and experimental results at the other gauge locations, which matches the displacement observations. Apart from the difference in magnitude, the simulated strains do not completely capture the relaxation behavior observed in the measurements. For example, during the 20-minute pressure hold at 2400 Pa (between approximately 2500 and 3700 seconds), the strain measured by gauges 'A' and 'L' increased by 2.0×10^{-9}; whereas, the simulation predicted an increase of 2.0×10^{-10}. Additionally, the difference in strain at the end of the first 1000 Pa pressure hold (around 1900 seconds) and the start of the second 1000 Pa hold (around 4600 seconds) is 5.8×10^{-5} and 3.0×10^{-6} for the measured and simulated strains, respectively.

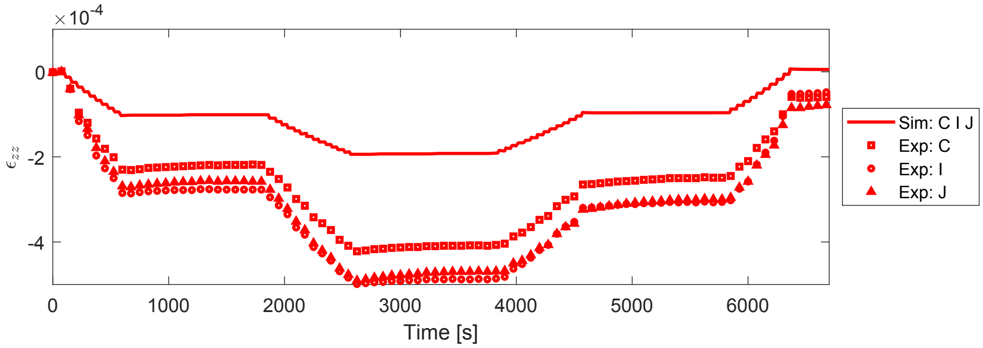

Figure 5-17: Comparison of strains in z-direction between simulation (Sim) and experiment (Exp) for each strain gauge in module 2.

In Figure 5-17, the experimental measurements of the z-strains are close in magnitude to suggest that the symmetry condition holds for the photovoltaic module. Gauge 'C' differs most from the other two, which could be a result of mounting the module to the test fixture. The simulated strain for these gauge locations tracks the same trend; however, the magnitude is about one-third that of the measured strains.

The third module was constructed to evaluate the effect of the junction box. Figure 5-18 and Figure 5-19 compare the x- and z-strains for Module 3. In Figure 5-18, the measurements in red are located in similar positions in the module; gauges 'B' and 'O' are on the side with the junction box, gauges 'G' and 'J' are not. Similarly, the measurements in blue are located in like positions, with gauges 'D' and 'M' located near the junction box.

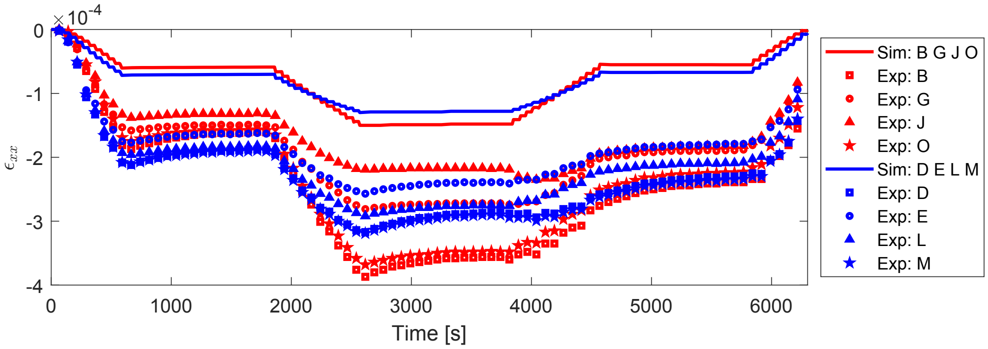

Figure 5-18: Comparison of strains in x-direction between simulation (Sim) and experiment (Exp) for each strain gauge in module 3.

In Figure 5-18, the measured strains at gauges 'B' and 'O' deviate little from each other in both magnitude and relaxation behavior, which suggests that the mechanical state of the module on either side of the junction box is identical. The strains at 'G' and 'J' differ more from each other but still follow similar trends. These two sets of gauges show that the strains near the junction box are higher than on the opposite side of the module. Compared to the experimental measurements, the simulated strains are much lower in magnitude, which is consistent with other observations. These trends also hold for gauges 'D', 'E', 'L', and 'M'.

In Figure 5-19, the red and blue measurements demarcate the gauge locations. Gauges 'A', 'P', 'C', and 'N' are located near the junction box; gauges 'I', 'F', and 'K' are on the opposite side of the module.

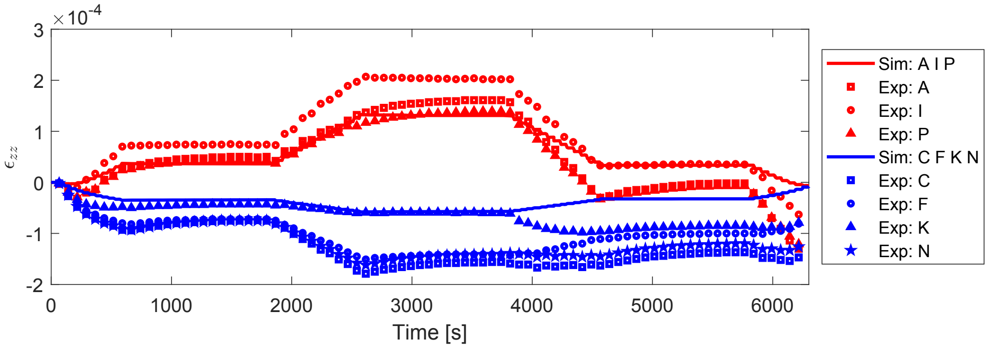

Figure 5-19: Comparison of strains in z-direction between simulation (Sim) and experiment (Exp) for each strain gauge in module 3.

For the z-strains in Module 3 shown by Figure 5-19, the gauges 'A' and 'P' near the junction box are nearly identical; whereas, the strain at gauge 'I' clearly deviates. There is also a large relaxation effect near the junction box at gauges 'A' and 'P' that is not present on the other side. At the other gauge location, we expected the strain at gauges 'F' and 'K' to follow identical paths; however, gauge 'F' aligns more closely with gauges 'C' and 'N' near the junction box. The simulated prediction of the z-strain at these locations matches the strain at gauge 'K' for the first 4000 seconds, but it does not capture the resulting relaxation behavior.

The last module is Module 4, which validates the use of dual-axis strain gauges and the viability of laminating strain gauges between the backsheet and encapsulant rather than directly on the photovoltaic cell. The strain gauge locations are given in Figure 2-3. In Figure 5-20, gauges 'C', 'D', and 'F' are laminated directly on the photovoltaic cells; whereas, gauge 'E' is laminated between the backsheet and the encapsulant.

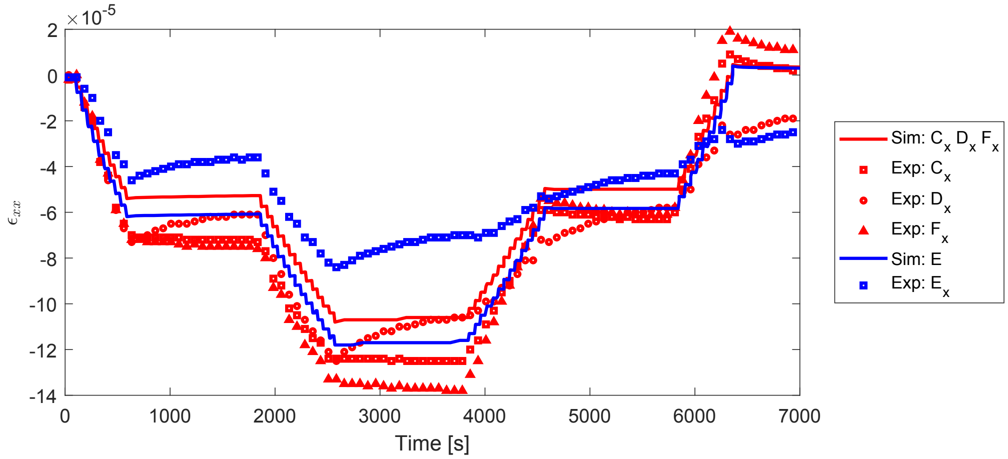

Figure 5-20: Comparison of strains in x-direction between simulation (Sim) and experiment (Exp) for each strain gauge in module 4.

The strain at gauges 'C', 'D', and 'F' shown in Figure 5-20 were expected to be identical; taking the average of their measurements, the maximum error between these measurements and the average is about 17%. Ideally, the strain at gauge 'E' would also be identical to the other gauges so that the mechanical state of the photovoltaic cell could be predicted without laminating a gauge directly to the cell. However, the strain predicted by gauge 'E' is far smaller in magnitude (about 33% smaller) and exhibits a more pronounced relaxation behavior, most likely attributed to the viscoelastic nature of both the EVA encapsulant and PET backsheet. This difference in strain will need to be accounted for in deployed modules.

In Figure 5-21, gauges 'A' and 'H' are in similar locations, but 'H' is laminated on the cell and 'A' is not. Gauges 'B' and 'G' are in symmetric locations, with each laminated on the cells. Gauges 'C', 'D' ('G' in Figure 2-3), 'E', and 'F' are the dual-axis gauges in like locations, with gauge 'E' laminated between the backsheet and encapsulant.

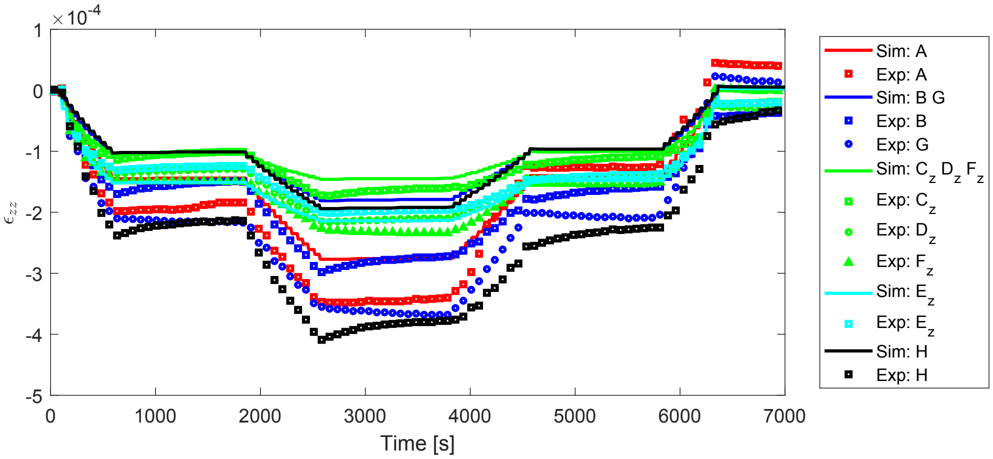

Figure 5-21: Comparison of strains in z-direction between simulation (Sim) and experiment (Exp) for each strain gauge in module 4.

As shown in Figure 5-21, the strain at gauge 'A' is comparable to gauge 'H', even though they are laminated in different layers. In this case, the gauge laminated to the cell (gauge 'H') experiences more relaxation than the one placed between the encapsulant and backsheet. The strain at gauges 'B' and 'G' differs by at most 30% near 4000 seconds since it appears the strain at gauge 'B' reduces and at gauge 'G' increases as the module relaxes. Finally, the strain at gauge 'E' aligns closely with gauges 'C', 'D', and 'F', despite being laminated in a different layer.

Based on the experimental strain measurements, Module 2 shows that the module generally deforms symmetrically as anticipated. Module 3, which tested for junction box effects, suggested that cells near the junction box experience larger strains than cells on the opposite side. The results from Module 3 also suggest that there is more relaxation occurring on the side with the junction box. This is attributed to the higher mismatch in stiffness between the more rigid junction box and more compliant module, leading to more initial strain on the cell. Lastly, the strains in Module 4 suggest that reported strains from strain gauges not directly adhered to a cell are noticeably distinct from adhered counterparts in the same module positions, and thus additional care is needed in interpreting their output as a true cell strain.

The simulations consistently underpredict the strain magnitude, likely resulting from the material model or geometric representation discrepancies. However, viscoelastic relaxation is significantly more observable, confirming that cell stress and strain quantities are affected by encapsulant viscoelasticity even if noticeable differences were not observable in module external displacements.

6. FURTHER STUDIES ON MATERIAL SELECTION

Considering the above difference in magnitudes of the displacements and strains between the simulation and the experiments, we conducted further studies on the influence of the material models on the module response. The EVA encapsulant is not the only material within the module that can be considered as viscoelastic; the silicone edge sealant also exhibits a time-dependent response.

To determine which module component has a greater influence on the magnitude and relaxation behavior of the displacements and strains, we conducted a pressure-loading study for several cases. The study used the same boundary conditions as the previous simulation, but the loading profile was truncated to only 20 minutes (1,200 seconds), as shown in Figure 6-1; the case details relating to the material models are summarized in Table 9.

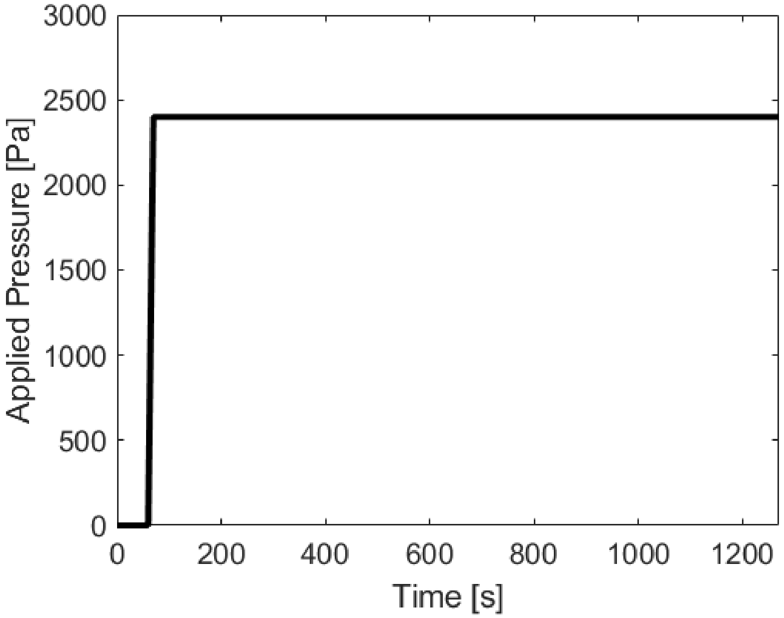

Figure 6-1: Loading profile used for case comparisons. Applied pressure is 0 Pa from 0 to 60 seconds. The pressure is ramped to 2400 Pa between 60 and 70 seconds. Finally, the pressure is held at 2400 Pa for 1200 seconds.

Table 9: Case descriptions for material selection investigation with an EVA encapsulant and PDMS edge sealant. "Updated" frame geometry refers to the frame without the lip feature as observed in Section 4.1; "Original" refers to the lip feature included in the frame geometry. Edge sealants with '*' use the material properties from Table 5.

Case Number	Material Model: EVA Encapsulant	Material Model: PDMS Edge Sealant	Frame Geometry
0	Viscoelastic	Elastic*	Updated
1	Elastic	Elastic	Updated

Case Number	Material Model: EVA Encapsulant	Material Model: PDMS Edge Sealant	Frame Geometry
2	Viscoelastic	Elastic	Updated
3	Elastic	Viscoelastic	Updated
4	Viscoelastic	Viscoelastic	Updated
5	Viscoelastic	Elastic*	Original

As noted in Section 4.1.1, excess overhang given by dimension ‘F’ in Figure 4-1 was included in the mesh used for the initial simulation that should have been omitted. This feature was corrected in the following module case comparisons, as indicated by the “Updated” label in Table 9; however, we also wanted to quantify the effect of removing this feature, so we compare the new and old geometries in Cases 0 and 5, respectively. The elastic material model for the PDMS edge sealant was left as listed in Table 5 to ensure that the only difference between the two cases is the frame geometry.

Cases 1 through 4 use a combination of viscoelastic and elastic material properties for EVA and PDMS. The viscoelastic models are taken from [11] for EVA and [13] for PDMS, with the SIERRA / Adagio input listed in Appendices B.4 and B.5. Reducing these models to an elastic material model that is still representative of the bulk behavior is not straightforward, since the moduli of viscoelastic materials is rate- and time-dependent. To determine the appropriate elastic modulus for each material, we conducted a stress-relaxation test, similar to the one shown in Appendix B.3, and computed the elastic modulus as the apparent modulus after 300 seconds of relaxation. This modulus was expected to give a reasonable estimate of the long-term response after loading. The corresponding elastic material properties for EVA and PDMS are given in Table 10.

Table 10: Elastic material properties for EVA and PDMS used in module case comparisons

Material	Poisson Ratio	Young’s Modulus [MPa]
EVA	0.48	9.09
PDMS	0.48	2.62

To evaluate the effect of the material model and geometric changes listed in Table 9, we take the displacement at sensor 80 and the strains at strain gauges ‘C’ and ‘E’ of Module 4, as given respectively in Figure 4-9 and Figure 2-3, as the response variables. Sensor 80 was chosen since it exhibits the largest displacement of the nine sensors, so it is expected that differences in magnitude resulting from the material properties and geometry will be seen most easily. Likewise, gauges ‘C’ and ‘E’ are located in the center of Module 4 provide information in both the x- and z-directions. Moreover, comparing gauges ‘C’ and ‘E’, which are placed in different layers of the laminate, will highlight any differences resulting from their placement on the cell directly or between the backsheet and encapsulant, respectively.

First, the displacement at sensor 80 for all six cases is given in Figure 6-2.

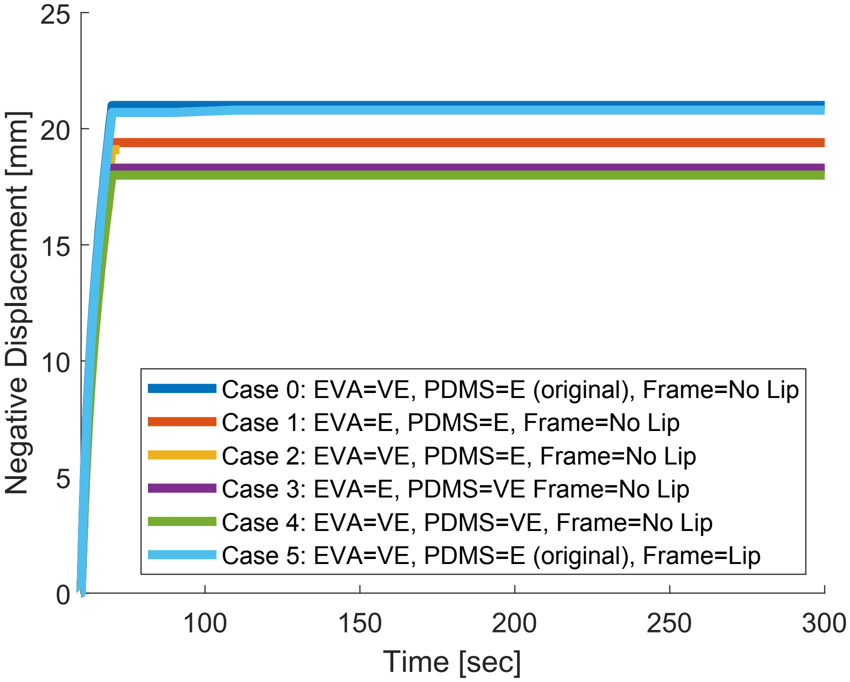

Figure 6-2: Comparison of case displacements at sensor 80 during 20-minute pressure hold at 2400 Pa.

Three distinct groupings appear in Figure 6-2: (1) cases 0 and 5, (2) case 1 and 2, and (3) cases 4 and 5. It should also be noted that case 2—that is, the case using the viscoelastic EVA and newly defined elastic PDMS—failed to complete the full duration of the simulation due to convergence issues. Still, it completed enough (70 seconds) to observe its grouping in relation to the other cases.

The first grouping is associated with the original material properties as listed in Table 5 and compare the effect of the lip-feature on the deflection. At 300 seconds, there is 0.9% difference between the displacements of the two cases, suggesting—at this location, at least—that the lip geometry does not have a considerable effect on the displacement as previously thought.

Cases 1 and 2 are different from 0 and 5 by the use of the new elastic modulus and Poisson ratio for PDMS. The new modulus is 3.5 times stiffer than the old modulus resulting in only 7.6% difference in displacement between case 0 and 1. It is difficult to quantify the exact difference in displacement between cases 1 and 2 since case 2 did not complete, but it is reasonable to conclude that any difference is attributed to the use of material model.

Cases 3 and 4 show the least amount of displacement compared to the other cases. This suggests that the elastic representation of PDMS as provided for cases 1 and 2 is more compliant than the viscoelastic material model, even though the elastic modulus was taken to be the modulus at 300 seconds. One possible explanation for this difference is the time-dependent behavior of the Poisson ratio, which will be discussed later.

In all five cases, it is worth observing that negligible relaxation behavior is observed during the constant pressure period, which is consistent with Section 5.1, although there is relaxation or other nonlinear phenomena occurring during the quick-loading phase.

Next, we compare the strains in the x-direction of gauges ‘C’ and ‘E’, which are laminated on the cell and between the backsheet and encapsulant, respectively, as given in Figure 2-3. First, the response of gauge ‘C’ is displayed in Figure 6-3.

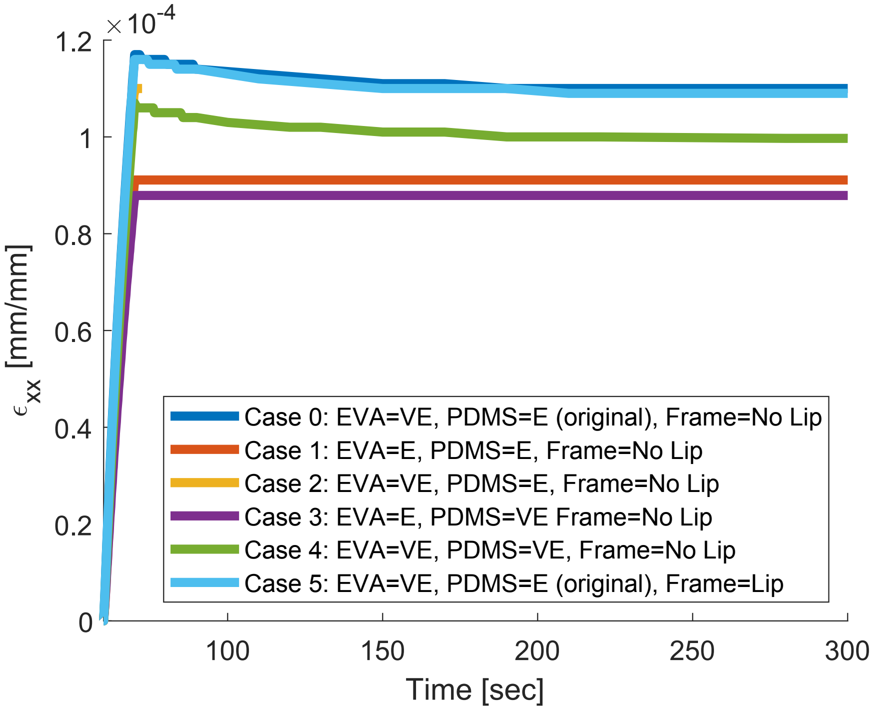

Figure 6-3: Comparison of case strains in x-direction at gauge 'C' during 20-minute pressure hold at 2400 Pa.

Unlike Figure 6-2, Figure 6-3 shows that all cases containing a viscoelastic component exhibit some degree of relaxation. Cases 0 and 5 suggest that the omission of the lip feature does not result in noticeably more strain in the x-direction at this location. We do notice, however, that the groupings of the remaining four cases shift: cases 1 and 3 versus cases 2 and 4. The collocation of cases 1 and 3 against cases 2 and 4 suggest that at this location the distinguishing material property is the elastic-viscoelastic material property distinction of the EVA. Again, the effective elastic modulus of the EVA was taken as the modulus at 300 seconds from the viscoelastic material model. Since this distinction exists, it is likely that the Poisson ratio or other factors contribute to the strain difference at this location.

Next, we observe the strains in the x-direction at gauge ‘E’, laminated between the backsheet and encapsulant, as shown in Figure 6-4.

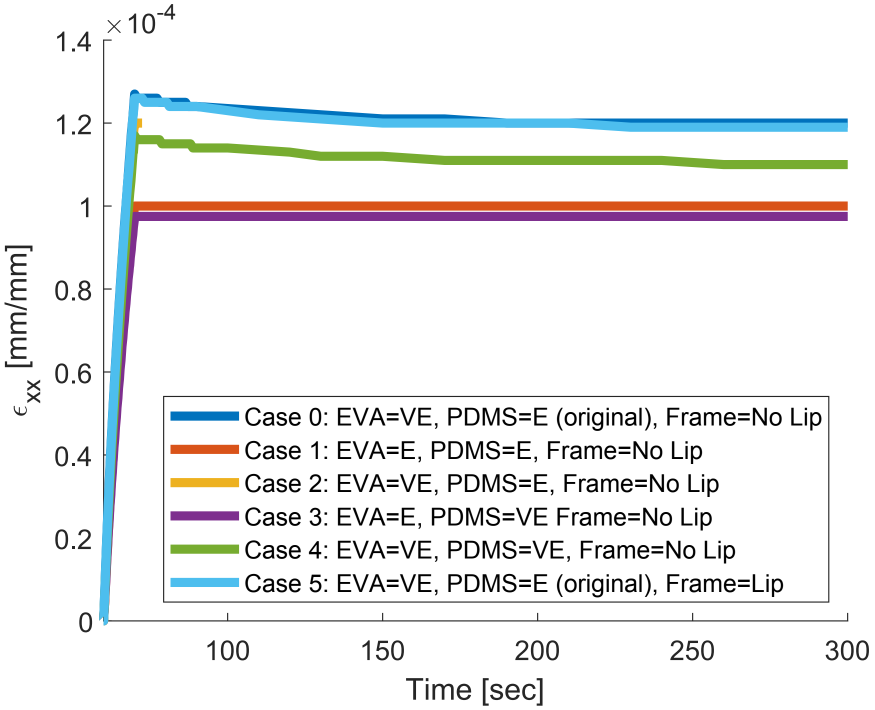

Figure 6-4: Comparison of case strains in x-direction at gauge 'E' during 20-minute pressure hold at 2400 Pa.

The grouping of the six cases in Figure 6-4 is identical to Figure 6-3, which suggests that the effect of the material properties used at this xz-location does not depend on the depth within the layers. All six cases predict about 20% higher strains than those at gauge 'C'. The curves from both gauge 'C' and 'E' also suggest that little, if any, relaxation behavior is observed by adding the viscoelastic contribution of the edge sealant, as seen in the difference between cases 1 and 3, or between cases 2 and 4.

Next, we look at the strains in the z-direction for the two gauges to compare the geometric, material property, and the gauge placement contributions on the strain response. Figure 6-5 shows the strains in the z-direction for gauge 'C', which is laminated on the cell located near the middle of the module.

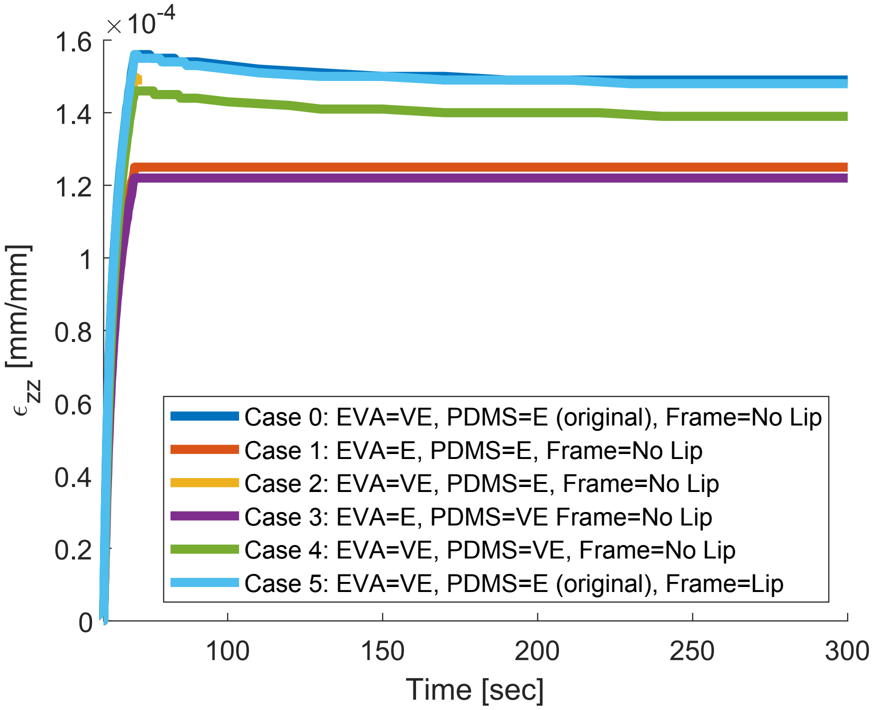

Figure 6-5: Comparison of case strains in z-direction at gauge 'C' during 20-minute pressure hold at 2400 Pa.

The strains in the z-direction predicted for the cell have identical groupings as the strains in the x-direction and the relaxation behavior is similar. We can again compare these trends to gauge 'E', which is laminated between the encapsulant and the backsheet near the center of the module, shown in Figure 6-6.

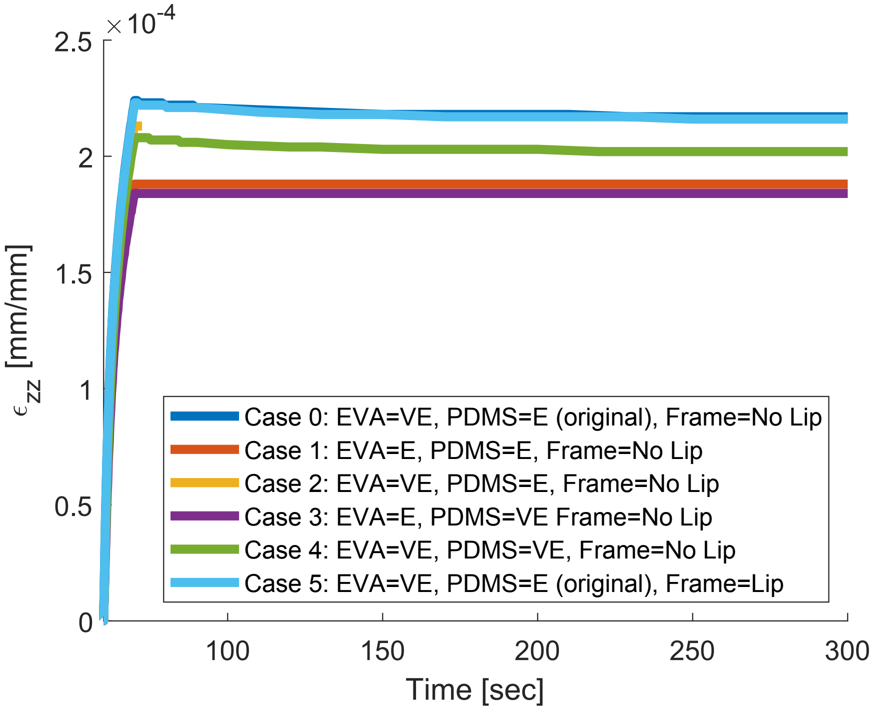

Figure 6-6: Comparison of case strains in z-direction at gauge 'E' during 20-minute pressure hold at 2400 Pa.

The strains predicted by gauge E shown in Figure 6-6 are all 25% larger than those predicted by gauge 'C'. The groupings are all consistent.

Since we had computed the elastic moduli for EVA and PDMS based on the long-term, 300-second behavior of the viscoelastic material, we had expected little difference between the elastic and viscoelastic models as the time approached 300 seconds. One possible source of this error is the change in effective Poisson ratio for the two materials over time. Based on [11] and [13], the instantaneous and long-term Poisson ratio for both materials can be computed from the bulk modulus, instantaneous shear modulus, and long-term shear modulus. These results are summarized in Table 11.

Table 11: Poisson ratios for EVA and PDMS as viscoelastic materials

Parameter	EVA	PDMS
ν_0	0.4899988	0.4980441
ν_∞	0.4999915	0.4995542

The Poisson values for both materials differ at all times compared to the prescribed $\nu = 0.48$ in the elastic material models. Although the difference between instantaneous- and long-term values is small, the ~4% difference between time dependent- and the time-independent values could be sufficient to explain some of groupings found in Figure 6-2 to Figure 6-6.

Overall, the comparison of the module response with different material models highlighted some key effects of viscoelastic contributions of the encapsulant and edge sealant. First, the viscoelastic material model for the encapsulant, as mentioned previously, is likely stiffer than the material used in experiments. Switching the material properties of the encapsulant with an EVA that exhibits more viscoelastic relaxation than used currently may reduce our errors between the simulations and experiments. Secondly, the short-time behavior of the PDMS edge sealant, as observed in the Prony series in [13], is not a likely source of the relaxation behavior observed over the twenty-minute periods where the pressure is held constant. The additional computational cost associated with implementing a viscoelastic edge sealant is not recommended.

Although not considered here, there are still other materials, like a viscoelastic PET polymer backsheet, or phenomena, like nonlinear contributions from friction between components, that may contribute to the relaxation behavior observed in the experiments.

7. CONCLUSIONS

Four photovoltaic modules were constructed for the purpose of validating an *in-situ* measurement technique of the module's mechanical state. One module was left un-instrumented to serve as a control, verifying that the strain gauge lamination process did not introduce significant defects in the remaining three modules. The instrumented modules were constructed to verify the symmetric deformation, the junction box effects, and the gauge placement within the lamina during a pressure-induced mechanical test. Displacement measurements were obtained using optical sensors and the strain gauges monitored the strain behavior during each test. The strain gauges showed variability in the outputs over time, suggesting that the measurements are likely sensitive to the lamination process. Recommendations were suggested for future photovoltaic module laminations.

High-fidelity finite-element simulations of a photovoltaic module were validated against the experimental *in-situ* measurements of the mechanical state. The simulations accounted for the viscoelastic behavior of the module encapsulant using the universal polymer model, implemented in SIERRA / Adagio, which was verified against results from literature. The results of the simulated pressure cycle predicted smaller displacements and strains than was measured experimentally. We posited two reasons for this discrepancy, including errors in the geometric representation of the module and differences in the material properties. It was determined that the implemented encapsulant material model exhibited less relaxation behavior than the actual material used in manufacturing the photovoltaic module. We expect that repeating the high-fidelity simulation with material properties for a more representative encapsulant would provide closer agreement with the experimental observations.

Six simulations were conducted to quantify the difference in response variables—namely, displacements and strains near the center of the module—for varying material properties and geometric features. Although errors in the geometric representation of the module existed, these further studies found that the geometric errors had less of an effect on the overall module response than did the selected material model and material properties of the encapsulant and edge sealant. We found that the modulus of the edge sealant contributes to the displacement and strain magnitudes but has little influence on the relaxation behavior at the tested time scales. Thus, an elastic material model for the edge sealant is suitable for the given photovoltaic module to reduce computational costs.

Overall, instrumenting a photovoltaic module with strain gauges was demonstrated as a method for obtaining the mechanical state during the tested pressure cycle. Although differences in both the magnitude and relaxation behavior of the displacements and strains persisted between the simulations and experiments, these errors can be minimized by more precise characterization of the material properties. Additional challenges were variability in measurements, possibly attributable to the manual construction techniques used. Nonetheless, with some process improvements, this method could potentially be expanded to predict the stress-strain response from other difficult-to-characterize environments that a photovoltaic module will encounter in its lifetime, including high-frequency cyclic pressure loadings, hailstone impacts, and abuse loading from transportation and installation environments.

REFERENCES

[1] A. Maes, J. Hartley, M. Rowell, C. Robinson, and T. Khraishi, "Instrumented Modules for Mechanical Environment Characterization and Simulation Model Validation," *2020 47th IEEE Photovoltaic Specialists Conference (PVSC)*, pp. 1525-1530, 2020, doi: 10.1109/PVSC45281.2020.9300468.

[2] N. Bosco, M. Springer, and X. He, “Viscoelastic Material Characterization and Modeling of Photovoltaic Module Packaging Materials for Direct Finite-Element Method Input,” IEEE J. Photovoltaics, vol. 10, no. 5, pp. 1424–1440, Sep. 2020, doi:10.1109/JPHOTOV.2020.3005086.

[3] A. El Amrani, A. Mahrane, F. Moussa, and Y. Boukennous, "Solar Module Fabrication," International Journal of Photoenergy, vol. 2007, no. 26610, Feb. 2007, doi:10.1155/2007/27610.

[4] A. Gabor, R. Janoch, A. Anselmo, J. Lincoln, H. Seigneur, and C. Honeker, "Mechanical Load Testing of Solar Panels - Beyond Certification Testing," 2016 IEEE 43rd Photovoltaic Specialists Conference (PVSC), pp. 3574-579, 2016, doi:10.1109/PVSC.2016.7750338.

[5] J. Hartley, M. Owen-Bellini, T. Truman, A. Maes, E. Elce, A. Ward, T. Khraishi, and S. Roberts, "Effects of Photovoltaic Module Materials and Design on Module Deformation Under Load," IEEE Journal of Photovoltaics, vol. 10, no. 3, pp. 838-843, May 2020, doi:10.1109/JPHOTOV.2020.2971139.

[6] Brightspot Automation LLC, “LoadSpot: Solar Panel Crack Detector & Mechanical Load Tester,” [Online]. Available: https://brightspotautomation.com/products/loadspot/. [Accessed: Mar. 25, 2022].

[7] HBM, “X280 Strain Gauge Adhesive for Use in Higher Temperatures,” Aug. 05, 2021. [Online]. Available: https://www.hbm.com/en/2960/x280-two-component-epoxy-resin-adhesive/. [Accessed: Mar. 25, 2022].

[8] Micro-Measurements, “General Information and Selection: Wire, Cable and Accessories.” Datasheet, Nov. 20, 2017.

[9] National Instruments, “NI-9237 C Series Strain/Bridge Input Module,” Datasheet, [Online]. Available: https://www.ni.com/en-us/support/model.ni-9237.html. [Accessed: Mar. 25, 2022].

[10] M. Skroch et al, “CUBIT Geometry and Mesh Generation Toolkit 16.02 User Documentation,” Sandia National Laboratories Report. Albuquerque, NM, 2021, SAND2021-12663 W

[11] M. Springer and J. Hartley, “Multi-Scale Modeling material properties” Email Communication, July. 14, 2020.

[12] F. Beckwith et al, “Sierra/Solid Mechanics 5.6 User’s Guide,” Sandia National Laboratories Report. Albuquerque, NM, 2022, SAND2022 3705

[13] K. Long and J. Brown, “A Linear Viscoelastic Model Calibration of Sylgard 184.,” SAND2017-4555R, 1365535, 652905, Apr. 2017. doi: 10.2172/1365535.

[14] HBM, “Y Series Universal Strain Gauges Datasheet” B4709-1.0 en. Datasheet.

APPENDIX A. STRAIN GAUGE DATASHEETS

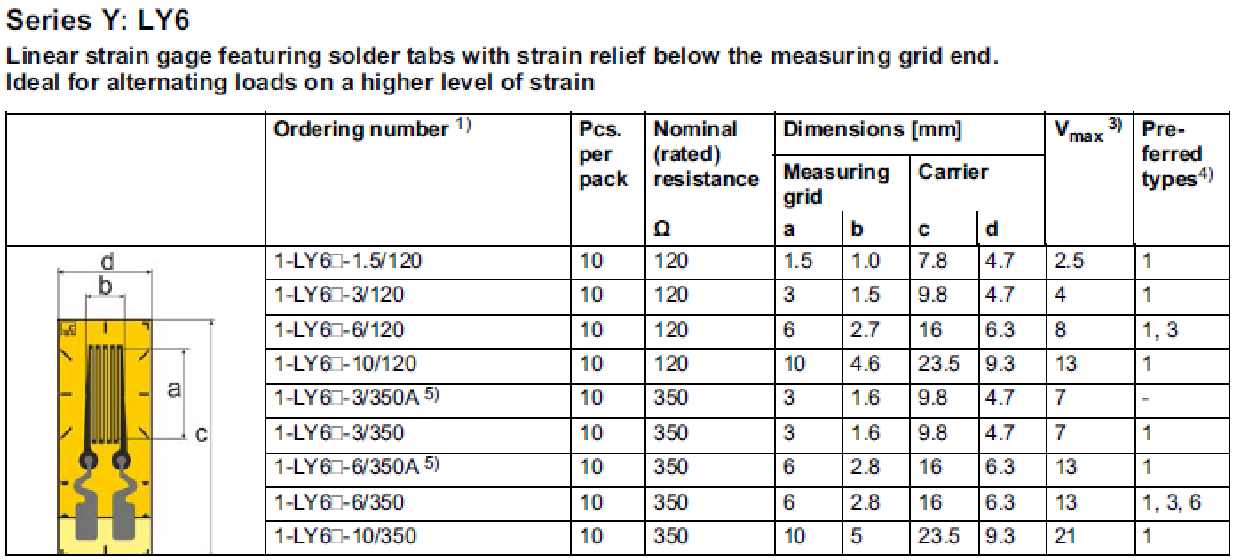

Series Y: LY6

Linear strain gage featuring solder tabs with strain relief below the measuring grid end.
Ideal for alternating loads on a higher level of strain

	Ordering number [1]	Pcs. per pack	Nominal (rated) resistance	Dimensions [mm]				V_{max} [3]	Pre-ferred types[4]
				Measuring grid		Carrier			
			Ω	a	b	c	d		
	1-LY6□-1.5/120	10	120	1.5	1.0	7.8	4.7	2.5	1
	1-LY6□-3/120	10	120	3	1.5	9.8	4.7	4	1
	1-LY6□-6/120	10	120	6	2.7	16	6.3	8	1, 3
	1-LY6□-10/120	10	120	10	4.6	23.5	9.3	13	1
	1-LY6□-3/350A [5]	10	350	3	1.6	9.8	4.7	7	-
	1-LY6□-3/350	10	350	3	1.6	9.8	4.7	7	1
	1-LY6□-6/350A [5]	10	350	6	2.8	16	6.3	13	1
	1-LY6□-6/350	10	350	6	2.8	16	6.3	13	1, 3, 6
	1-LY6□-10/350	10	350	10	5	23.5	9.3	21	1

Figure 7-1: Datasheet from HBM for linear strain gauges used in instrumented module [14].

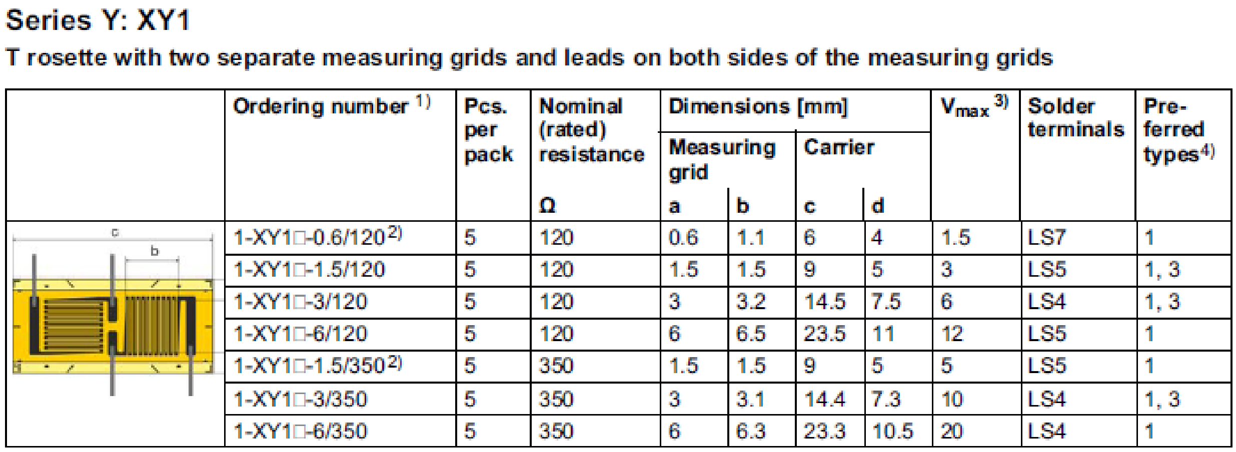

Series Y: XY1

T rosette with two separate measuring grids and leads on both sides of the measuring grids

	Ordering number [1]	Pcs. per pack	Nominal (rated) resistance	Dimensions [mm]				V_{max} [3]	Solder terminals	Pre-ferred types[4]
				Measuring grid		Carrier				
			Ω	a	b	c	d			
	1-XY1□-0.6/120[2]	5	120	0.6	1.1	6	4	1.5	LS7	1
	1-XY1□-1.5/120	5	120	1.5	1.5	9	5	3	LS5	1, 3
	1-XY1□-3/120	5	120	3	3.2	14.5	7.5	6	LS4	1, 3
	1-XY1□-6/120	5	120	6	6.5	23.5	11	12	LS5	1
	1-XY1□-1.5/350[2]	5	350	1.5	1.5	9	5	5	LS5	1
	1-XY1□-3/350	5	350	3	3.1	14.4	7.3	10	LS4	1, 3
	1-XY1□-6/350	5	350	6	6.3	23.3	10.5	20	LS4	1

Figure 7-2: Datasheet from HBM for two-directional strain gauge used in instrumented module [14].

APPENDIX B. VISCOELASTIC MATERIAL VALIDATION

B.1. Basics of Viscoelasticity: SIERRA/Adagio Universal Polymer Model

The Universal Polymer Model (UPM) material model in SIERRA/Adagio was used to represent the viscoelastic material behavior of the EVA encapsulant [8]. The UPM requires the information of the glassy and rubbery shear moduli (G_G, G_∞), glassy and rubbery bulk moduli (K_G, K_∞), the Prony spectra time, volumetric relaxation, and shear relaxation weights (τ_i, k_i, g_i), glassy and rubbery thermal expansion coefficients (δ_G, δ_∞), material clock parameters (C_1, C_2, C_3, C_4), and a reference temperature (θ_{ref}).

It is generally assumed that most nearly incompressible viscoelastic materials exhibit bulk relaxation behavior of order many times fewer than the shear relaxation behavior. Thus, it is reasonable to neglect bulk relaxation behavior by setting the rubbery bulk modulus equal to the glassy bulk modulus. The shear relaxation parameters and shear moduli are then obtained by optimizing the n-term Maxwell model coefficients to fit the shear modulus master curve using nonlinear regression. The maximum number of terms is determined by the number of logarithmic decades of test data that is available in the master curve. For example, a frequency-based master curve ranging between 1 Hz and 1000 Hz spans three decades; thus, n can be at most three. Adding more terms to the Prony series fit increases the accuracy of the fit, but also increases the computational cost.

For linear thermoviscoelastic materials—that is, for materials whose relaxation behavior is temperature dependent but not deformation dependent—, C_3 and C_4 are set to zero. The only parameters that describe the temperature dependence of these materials are θ_{ref}, C_1 and C_2. The thermal expansion coefficients can be set either by a single value or as a function of strain.

B.2. Viscoelastic Material Model for EVA: Prony Series

The EVA viscoelastic material model was given by [2], and the lower-fidelity Prony series was obtained in private communication [11]. The 22-term Prony series is given below in Table 12. The time constants, τ_i, span the frequency range of the shear modulus test data; the shear modulus relaxation coefficients, g_i, which are normalized, provide information on the magnitude of relaxation that occurs at each τ_i.

Table 12: 22-Term Prony Series for EVA

#	τ_n	g_n
1	1.0E-10	4.72E-02
2	1.0E-08	8.39E-02
3	1.0E-06	1.16E-01
4	1.0E-04	1.66E-01
5	1.0E-02	2.09E-01
6	1.0E+00	2.00E-01
7	1.0E+02	1.06E-01
8	1.0E+04	3.90E-02
9	1.0E+06	1.35E-02
10	1.0E+08	5.69E-02
11	1.0E+10	3.00E-03
12	1.0E+12	1.84E-03
13	1.0E+14	1.58E-03
14	1.0E+16	1.34E-03
15	1.0E+18	9.86E-04
16	1.0E+20	9.03E-04
17	1.0E+22	7.45E-04
18	1.0E+24	6.40E-04
19	1.0E+26	5.74E-04
20	1.0E+28	5.34E-04
21	1.0E+30	3.11E-04
22	1.0E+32	5.12E-04

B.3. Stress-Relaxation Validation

A stress-relaxation experiment was conducted in [2] to verify that the high-fidelity, 46-term Prony series and the WLF parameters could predict the relaxation behavior of EVA subjected to uniaxial strain at various temperatures. The rectangular EVA specimen was extended to 1.2% uniaxial strain and held for 300 seconds; the force required to maintain the constant strain was recorded. The time versus force curve was published in [2], but the specimen dimensions were not provided. In private communication, we obtained the time versus shear modulus curve of the relaxation test from Nick Bosco, which eliminates the geometric dependence on the curve's magnitude.

In [2], the experimental results of the time versus force were compared against the simulation results obtained by using the 44-term Prony series, which showed good agreement. However, we needed to validate the lower-fidelity, 22-term Prony series against the same data to determine if it also provides a good fit. Simulations of the uniaxial stress-relaxation test were carried out in SIERRA/Adagio at the four test temperatures used in [2]: $T = 2°C$, $T = 20°C$, $T = 40°C$, and $T = 60°C$. The extension of the rectangular EVA specimen resulting from a step-displacement is shown in Figure 7-33.

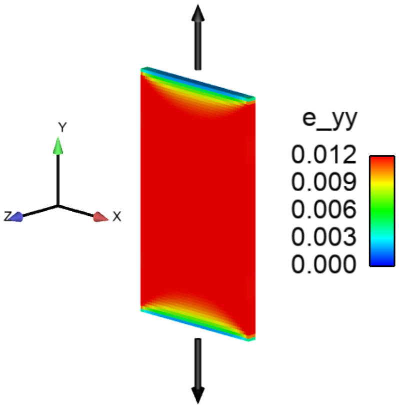

Figure 7-3: Uniaxial stress-relaxation simulation. Contour shows engineering strain in vertical direction.

The reaction force at each time-step was divided by the cross-sectional area to give Young's modulus, which was in turn converted to shear modulus using the Poisson value listed previously in Table 6. The resulting time versus shear modulus relaxation curves obtained by the simulations are given in Figure 7-44, which are plotted against the published data from [2].

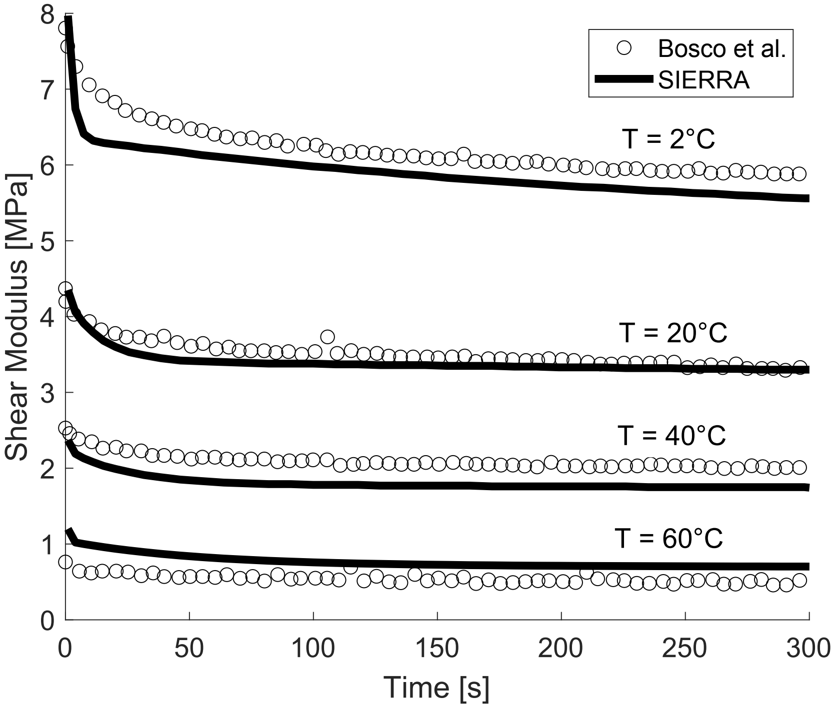

Figure 7-4: Time versus shear modulus relaxation behavior for experimental results (Bosco et al. [2]) and simulation (SIERRA), conducted at four temperatures on a rectangular EVA specimen.

Overall, the results from the relaxation simulations show adequate agreement with experimental results obtained by Bosco et al.; the material is softer—or more rubbery—at higher temperatures, most of the relaxation occurs within the first minute for tests at or above room temperature, and after which the shear modulus is almost constant. Discrepancies between the experimental and simulation results can be attributed mostly to the lower-fidelity material description, but since the overall behavior is captured, we conclude that the 22-term Prony series is an appropriate viscoelastic material definition for the EVA.

B.4. EVA Viscoelastic Material Model Script: SIERRA/Adagio

Below is an excerpt of the SIERRA/Adagio script that defines the viscoelastic material model for EVA, adapted from [2] and [11].

```
# Properties from Bosco et al. (2020), Viscoelastic Material Characterization and Modeling of
#       Photovoltaic Module Packaging Materials for Direct Finite-Element Method Input
begin property specification for material EVA_UPM

    density       = 931 # typical literature
    thermal log strain function = evastrain # zero polynomial for 0 thermoelastic strain

    begin parameters for model universal_polymer
```

```
bulk modulus   = 30732243333  # Pa
shear modulus  =   618770000  # Pa
wwbeta 1 = 0.3
wwtau 1  = 0.0001
wwbeta 2 = 0.0
wwtau 2  = 0.0
spectrum start time = 0
spectrum end time = 0
log time increment = 0
bulk glassy 0 = 30732243333   # Pa
bulk glassy 1 =  0
bulk glassy 2 =  0
bulk rubbery 0 = 30732243333  # Pa
bulk rubbery 1 = 0
bulk rubbery 2 = 0

volcte glassy 0 = 0
volcte glassy 1 = 0
volcte glassy 2 = 0
volcte rubbery 0 = 0
volcte rubbery 1 = 0
volcte rubbery 2 = 0

shear glassy 0 = 618770000    # Pa, G_0
shear glassy 1 = 0
shear glassy 2 = 0
shear rubbery 0 = 521217.14   # Pa, G_inf
shear rubbery 1 = 0
shear rubbery 2 = 0
reference temperature = 243   # K, from log_at vs T fit
wlf c1 = 645.99              # []
wlf c2 = 2122.36              # K
clock c1 = 0
clock c2 = 0
clock c3 = 0
clock c4 = 0
clock c5 = 0
clock c6 = 0
filler vol fraction = 0
stress free temperature = 358 # K (85 C)

#  these are G_n relaxation times, Bosco low-fidelity Prony series
```

```
relax time 1 = 1.00000e-10
relax time 2 = 1.00000e-08
relax time 3 = 1.00000e-06
relax time 4 = 1.00000e-04
relax time 5 = 1.00000e-02
relax time 6 = 1.00000e+00
relax time 7 = 1.00000e+02
relax time 8 = 1.00000e+04
relax time 9 = 1.00000e+06
relax time 10 = 1.00000e+08
relax time 11 = 1.00000e+10
relax time 12 = 1.00000e+12
relax time 13 = 1.00000e+14
relax time 14 = 1.00000e+16
relax time 15 = 1.00000e+18
relax time 16 = 1.00000e+20
relax time 17 = 1.00000e+22
relax time 18 = 1.00000e+24
relax time 19 = 1.00000e+26
relax time 20 = 1.00000e+28
relax time 21 = 1.00000e+30
relax time 22 = 1.00000e+32

# these are G_n relaxation moduli, Bosco low-fidelity Prony series
f2 1  =  4.717590E-02
f2 2  =  8.393374E-02
f2 3  =  1.163279E-01
f2 4  =  1.656301E-01
f2 5  =  2.093154E-01
f2 6  =  2.001846E-01
f2 7  =  1.059250E-01
f2 8  =  3.903487E-02
f2 9  =  1.348714E-02
f2 10 =  5.687239E-03
f2 11 =  3.000164E-03
f2 12 =  1.843053E-03
f2 13 =  1.577686E-03
f2 14 =  1.341054E-03
f2 15 =  9.857247E-04
f2 16 =  9.031648E-04
f2 17 =  7.447443E-04
f2 18 =  6.402500E-04
```

```
        f2 19 =  5.740986E-04
        f2 20 =  5.343953E-04
        f2 21 =  3.106288E-04
        f2 22 =  5.118922E-14

    end parameters for model universal_polymer

end property specification for material EVA_UPM
```

B.5. PDMS Viscoelastic Material Model Script: SIERRA/Adagio

Below is an excerpt of the SIERRA/Adagio script that defines the viscoelastic material model for PDMS, adapted from [10].

```
# Properties from Long & Brown (2017), A Linear Viscoelastic Model Calibraion of Sylgard 184
begin property specification for material PDMS_UPM

    density = 1003  ## kg/m^3

    begin parameters for model universal_polymer
        bulk modulus   = 0.92e9    # Pa
        shear modulus  = 0.61e6    # Pa

        wwbeta 1 = 0.14   # []
        wwtau 1  = 6.00   # s
        wwbeta 2 = 0.00   # []
        wwtau 2  = 0.00   # s

        spectrum start time  = 0.0
        spectrum end time    = 0.0
        log time increment   = 0.0

        bulk glassy 0   = 0.92e9    # Pa
        bulk glassy 1   = 0.0
        bulk glassy 2   = 0.0
        bulk rubbery 0  = 0.92e9    # Pa
        bulk rubbery 1  = 0.0
        bulk rubbery 2  = 0.0

        volcte glassy 0   = 0.0    # (changed from 0.00017 1/K)
        volcte glassy 1   = 0.0
```

```
volcte glassy 2   = 0.0
volcte rubbery 0  = 0.0    # (changed from 0.00060 1/K)
volcte rubbery 1  = 0.0
volcte rubbery 2  = 0.0

shear glassy 0    = 3.621783e6   # Pa
shear glassy 1    = 3.662777e3   # Pa/K
shear glassy 2    = 0.0
shear rubbery 0   = 8.387312e5   # Pa
shear rubbery 1   = 3.662777e3   # Pa/K
shear rubbery 2   = 0.0

reference temperature = 303.15 # K

wlf c1   = 20.003660    # []
wlf c2   = 418.862744   # K
clock c1 = 0.0
clock c2 = 0.0
clock c3 = 1000         # 1/K
clock c4 = 0.0
clock c5 = 0.0
clock c6 = 0.0

filler vol fraction = 0.0
stress free temperature = 293.15   # K (should be about room temp)

# Direct Prony Series Representation of the Shear Spectrum
relax time 1 = 1.00000e-06
relax time 2 = 3.16000e-06
relax time 3 = 1.00000e-05
relax time 4 = 3.16000e-05
relax time 5 = 1.00000e-04
relax time 6 = 3.16000e-04
relax time 7 = 1.00000e-03
relax time 8 = 3.16000e-03
relax time 9 = 1.00000e-02
relax time 10 = 3.160000e-02
relax time 11 = 1.00000e-01
relax time 12 = 3.16000e-01
relax time 13 = 1.00000e+00
relax time 14 = 3.16000e+00
relax time 15 = 1.00000e+01
```

```
relax time 16 = 3.16000e+01
relax time 17 = 1.00000e+02
relax time 18 = 3.16000e+02
relax time 19 = 1.00000e+03
relax time 20 = 3.16000e+03

f2 1     = 5.06098e-01
f2 2     = 0.00000e+00
f2 3     = 1.27611e-01
f2 4     = 7.55463e-02
f2 5     = 6.61488e-02
f2 6     = 5.68130e-02
f2 7     = 4.20298e-02
f2 8     = 3.56497e-02
f2 9     = 2.57836e-02
f2 10     = 1.89884e-02
f2 11     = 1.26279e-02
f2 12     = 1.09535e-02
f2 13     = 3.99764e-03
f2 14     = 6.17595e-03
f2 15     = 2.26342e-03
f2 16     = 2.91730e-03
f2 17     = 2.04165e-03
f2 18     = 1.72507e-03
f2 19     = 8.52181e-04
f2 20     = 1.77735e-03

f1 1     = 5.06098e-01
f1 2     = 0.00000e+00
f1 3     = 1.27611e-01
f1 4     = 7.55463e-02
f1 5     = 6.61488e-02
f1 6     = 5.68130e-02
f1 7     = 4.20298e-02
f1 8     = 3.56497e-02
f1 9     = 2.57836e-02
f1 10     = 1.89884e-02
f1 11     = 1.26279e-02
f1 12     = 1.09535e-02
f1 13     = 3.99764e-03
f1 14     = 6.17595e-03
f1 15     = 2.26342e-03
```

```
        f1 16    = 2.91730e-03
        f1 17    = 2.04165e-03
        f1 18    = 1.72507e-03
        f1 19    = 8.52181e-04
        f1 20    = 1.77735e-03
    end parameters for model universal_polymer

end property specification for material PDMS_UPM
```

This page left blank

DISTRIBUTION

Email—Internal

Name	Org.	Sandia Email Address
Christine Roberts	1512	ccrober@sandia.gov
Scott Roberts	1513	sarober@sandia.gov
James Hartley	1514	jkyuan@sandia.gov
Brantley Mills	1514	bramill@sandia.gov
Matthew Phillips	1514	mrphill@sandia.gov
Leslie Phinney	1514	lmphinn@sandia.gov
Cliff Hansen	8812	cwhanse@sandia.gov
Bruce King	8924	bhking@sandia.gov
Charles Robinson	8924	cdrobin@sandia.gov
Josh Stein	8824	jsstein@sandia.gov
Technical Library	01977	sanddocs@sandia.gov

Email—External [redacted]

Name	Company Email Address	Company Name
Matthew R. Phillips	mphilli2@ncsu.edu	North Carolina State University

This page left blank